2012-03-14

Application of High Resolution Electron Backscatter Diffraction(HR-EBSD) Techniques to Twinning Deformation Mechanism in AZ31 Magnesium Alloy

Ali Khosravani
Brigham Young University - Provo

Application of high Resolution Electron Backscatter Diffraction (HR-EBSD) Techniques to Twinning Deformation Mechanisms in AZ31 Magnesium Alloy

Ali Khosravani

A thesis submitted to the faculty of
Brigham Young University
in partial fulfillment of the requirements for the degree of

Master of Science

David T. Fullwood, Chair
Mike P. Miles
Eric R. Homer

Department of Mechanical Engineering
Brigham Young University
April 2012

ABSTRACT

Application of high Resolution Electron Backscatter Diffraction (HR-EBSD) Techniques to Twinning Deformation Mechanisms in AZ31 Magnesium Alloy

Ali Khosravani
Department of Mechanical Engineering, BYU
Master of Science

The application of high resolution electron backscatter diffraction (HR-EBSD) techniques has been used in order to study the evolution of geometrically necessary dislocation (GND). The tested materials were taken from AZ31 magnesium sheet which had strong basal texture. Because of low symmetry of the magnesium crystal lattice, the von Mises criteria cannot be satisfied by the three independent, easily activated, basal slips. The strain along the c-axis of the crystal must be accommodated by either twinning and/or <c+a> slip systems. HR-EBSD data was taken in order to investigate these phenomena. The HR-EBSD results were post processed in order to resolve total GND density onto the observed possible slip systems.

The first chapter of the investigation focused on the correlation between resolved GNDs with tensile twin nucleation, and the subsequent propagation path in the microstructure. For this purpose, 2.5 % strain was applied in a uniaxial compression test along the transverse direction (TD). Several fine scan were done at the boundaries where twin formed. The results show that in order for a twin to nucleate spontaneously at the grain boundaries, two criteria should generally be met: high angle grain boundaries (35-45°) and pile ups of basal slip system in neighboring grain at the other side of the boundary. Furthermore, once nucleation has initiated, twin propagation can occur through low angle grain boundaries (15-25°); if a twin reaches a high angle boundary, it will generally terminate at the boundary at low strain levels. A twin may pass through high angle boundaries with further deformation.

In the second chapter, deformation of the AZ31 magnesium alloy was study for different strain paths. For this purpose, compression and tension in-situ tests were done and the texture and GND evolutions were investigated. The results show that the load paths, compression and tension, evolve the microstructure in different ways. Massive twin fractions were formed in compression, and higher GND contents were observed in tension tests. It was observed that at higher strain levels GND contents are roughly independent of the initial texture but the activation of slip systems at low strain strongly depends on initial structure. If the samples were loaded along RD, GND density increased sharply at low strain. In contrast, for the samples loaded along TD, GND increased moderately. A small amount of repetition is apparent in the two parts of the thesis due to them being formatted for individual publication as journal papers.

Keywords: Ali Khosravani, EBSD, AZ31 magnesium alloy, tension twins, in-situ tension and compression tests.

ACKNOWLEDGEMENTS

This research project would not have been possible without the support of many people. The author wishes to express his gratitude to his supervisors, Prof. Fullwood and Prof. Adams who were abundantly helpful and offered invaluable assistance, support and guidance. Deepest gratitude are also due to the members of the supervisory committee, Dr. Miles and Dr. Homer without whose knowledge and assistance this study would not have been successful. Special thanks also to all my friends, especially group members; Travis Rampton, Tim Ruggles, Jay Basinger, Ribeka Takahashi, Samikshya Subedi and Caroline Sorensen for invaluable assistance.

The author would also like to convey thanks to Dr. Mishra in GM R&D department for providing the material and financial support and laboratory facilities. The author wishes to express his love and gratitude to his beloved families; for their understanding and endless love, through the duration of his studies.

This material is based upon work supported by the National Science Foundation under Grant No. 0928923. Any opinions, findings, and conclusions or recommendations expressed in this material are those of the author and do not necessarily reflect the views of the National Science Foundation.

TABLE OF CONTENTS

LIST OF TABLES

LIST OF FIGURES

1 NUCLEATION AND PROPAGATION OF $\{10\bar{1}2\}$ TWINS IN AZ31 MAGNESIUM ALLOY

Abstract

Nucleation and propagation of tensile twins in AZ31 magnesium alloy are investigated using high-resolution electron backscatter diffraction (HREBSD) techniques. Both types of nucleation, slip-assisted and twin-assisted nucleation, have correlations with type <a> slip system activities. Slip-assisted nucleations mostly happen at high-angle grain boundaries where type <a> slip systems in an adjacent grain accumulate in the vicinity of that boundary. In contrast, twin-assisted twinning is caused by twin propagation phenomena when one twin in a neighboring grain reaches a low-angle grain boundary and dislocation pile up at the twin tip can form another twin in the neighboring grain. However, at low strain levels, pile up of <a> slip systems at a twin tip is not sufficient to allow the twin to transmit from one grain to another one through high-angle boundaries.

1.1 Introduction

Recent advantages in EBSD provide not only higher spatial resolution but more information about geometrically necessary dislocations (GND) from the surface of the material[1]. In this

study, this technique is used on AZ31 magnesium alloy to find correlations between tensile twin nucleation and propagation, with resolved GND content in the microstructure.

Formability of Mg alloys at ambient temperature is poor due to the insufficient number of active slip systems in the HCP lattice [2-7]. According to the von-Mises criterion, five independent slip systems are required for plastic deformation of polycrystalline materials. Hence deformation twinning plays an important role in plastic deformation of magnesium alloys [3, 8-11]. The most important available slip systems in magnesium alloys are basal <a> slip, prismatic <a> slip, pyramidal <a> (type I) slip and pyramidal <c+a> (type II) slip. Deformation studies on Mg alloy single crystals and polycrystals at room temperature showed that the critical resolved shear stress (CRSS) for basal slip is significantly lower than for non-basal slip [2, 8, 9, 12-15]. However, for strain accommodation along the c-axis, either <c+a> slip and / or mechanical twinning is required [2, 9, 16]. In contrast to dislocations which can move in two directions in the slip plane, twinning can happen in only one direction in the relevant plane; therefore, if the applied load is in an unfavorable condition for twin nucleation, <c+a> slip plays important role in deformation in order to arrive at the required five independent slip systems [2-5].

Several researchers have been seen activity of non-basal slip at room temperature. Koike et al [4, 5] showed that non-basal slip is needed in the vicinity of grain boundaries in order to maintain strain compatibility, and this compatibility stress causes nucleation of twins or activation of <c+a> slip systems; otherwise fracture would occur along grain boundaries. Keshavarz et al [12] observed the presence of prismatic slip within the grain far from grain boundaries and showed that non-basal slip could happen, not only at the grain boundary, but also inside the grains. Agnew et al [14, 16], with experiments and simulations involving the ECAE process, showed that in AZ31 and AZ80 the dominant slip system is basal; and also that there

exists a small portion of <a> prismatic and <c+a> pyramidal modes. However, they reported that at room temperature prismatic slip is the most active non-basal slip system.

1.2 Materials and methods

1.2.1 Experimental procedure

The material investigated in this study was a hot rolled AZ31 Mg alloy plate, which was homogenized at 350 C for 1 h and cooled to room temperature in the furnace. The twin-free equi-axed grain microstructure and the alloy's initial texture are presented in Fig. 1-4(a). The average linear intercept grain size is~10μm. A compression cube of $3mm \times 4mm \times 3mm$ was machined from the homogenized plate by using wire EDM to avoid any residual stress during cutting; then for EBSD scan preparation the sample was mounted in cold resin and polished. The sample preparation procedure was mechanical polishing followed by OP-S colloidal silica slurry which provides high quality surface finishing for EBSD. The sample was etched with a solution of 60% ethanol, 20% distilled water, 15% acetic acid and 5% nitric acid. Using a focused ion beam (FIB), Platinum fiducial marks were deposited on the sample's surface to measure local strain in the scan area. The sample was compressed along TD up to 2.5% strain.

Automatic EBSD scans were performed using the FEI-Helios NanoLab^{TM} 600i SEM equipped with OIM^{TM} data acquisition software and a high-speed Hikari^{TM} camera. In order to get dislocation maps, the EBSPs (electron backscattered patterns) were saved for all the scan points and later they were post-processed. Regular square grid scans were used to examine $100 \times 100\ \mu m^2$ with a 200 nm step size. The data with a confidence index < 0.07 were filtered out for texture analysis using TSL OIM software. For dislocation studies, several finer scans with

the step size of 100nm were performed at the border of the area in which twin nucleation occurred.

1.2.2 Methodology

Using high-resolution electron backscatter diffraction (HREBSD) techniques, near-surface geometrically necessary dislocation (density) tensors can be recovered from lattice distortion measurements. The principal and the method are described by Gardner et al [1]. The dislocation tensor's component can be extracted following the approach of Nye and Krö̈ner [17, 18]:

$$\boldsymbol{\alpha_{ik} = k_{ki} - \delta_{ki} k_{mm} - \epsilon_{klj} \frac{\partial \varepsilon_{ij}^{el}}{\partial x_l}} \qquad \textbf{1-1}$$

Where $\alpha_{ij}, k_{ij}, and\ \varepsilon_{ij}^{el}$ are the components of dislocation, lattice curvature, and the elastic strain tensors respectively [17]. If the elastic strain gradient term is considered to be negligible, this equation becomes

$$\boldsymbol{\alpha_{ik} = k_{ki} - \delta_{ki} k_{mm}} \qquad \textbf{1-2}$$

Having only 2-D scans, and hence only gradients in the plane of the surface of the sample, only 6 components of lattice curvature can be obtained. Using Eq. (2) only five components of dislocation tensor can be derived as shown in Eq. (3):

$$\boldsymbol{\alpha_{ij}} = \begin{bmatrix} - & \boldsymbol{\alpha_{12}} & \boldsymbol{\alpha_{13}} \\ \boldsymbol{\alpha_{21}} & - & \boldsymbol{\alpha_{23}} \\ - & - & \boldsymbol{\alpha_{33}} \end{bmatrix} \qquad \textbf{1-3}$$

The total dislocation density tensor may also be thought of as a sum over individual dislocation densities ρ^t from different dislocation types (t), each characterized by Burgers vector $\vec{b}^t$ and line vector $\vec{l}^t$ by considering all possible independent-slip systems:

$$\boldsymbol{\alpha_{ij} = \sum_{t=1}^{N} b_i^t l_j^t \rho^t} \qquad \textbf{1-4}$$

In order to solve for the dislocation activity on each slip system, ρ^t , an additional constraint must be added to this equation system, for example by minimizing the total dislocation density or line energy [17, 19].

In order to follow this process and subsequently attribute dislocation activity to <a> and <c+a> types, we first identify the independent slip systems that can be activated in magnesium alloys. All possible slip systems are illustrated in Fig. 1-1. The numbers of slip systems are listed by type in Table 1.1. The number of possible dislocation types depends on the geometry of the crystalline lattice and the particular dislocation characters (edge, screw). It was observed that the <c+a> dislocations are stable in screw form but unstable in edge orientation; and it is reported that the number of independent <c+a> slip systems is 5 [20]. As shown in Table 1 there are four independent slip systems for which both screw type and edge type are stable. Therefore 13 independent slip systems can be activated in magnesium alloys. Applying these 13 slip systems in Eq. (1-4) (i.e N=13), we obtain a set of 5 equations with 13 unknowns. A unique solution set for dislocation densities can be obtained only by adding additional constraints. In order to resolve total dislocation density in Eq. (1-4) into different slip systems, an additional function $f(\rho_1, \rho_2, \dots, \rho_N)$ is required to be minimized.

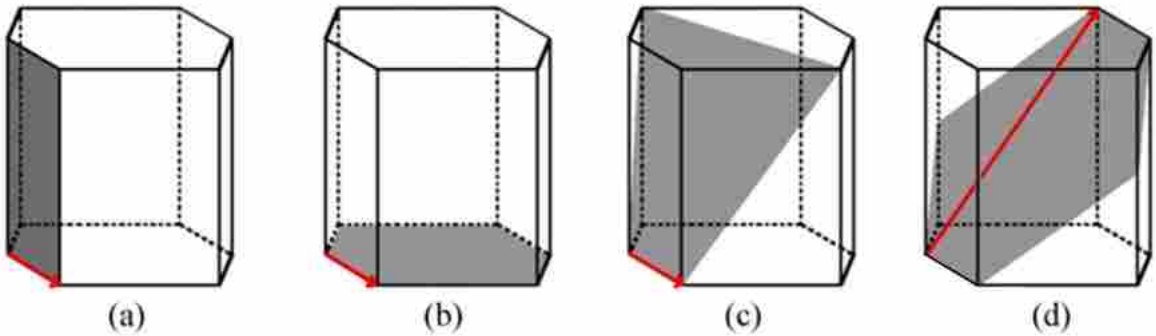

Figure 1-1. Possible slip systems: (a) <11$\bar{2}$0> {10$\bar{1}$0} prismatic, (b) <11$\bar{2}$0> (0001) basal, (c) <11$\bar{2}$0> {10$\bar{1}$1} pyramidal, and (d) <11$\bar{2}$2> {10$\bar{1}$2} pyramidal

Table 1-1. Numbers of total and independent slip systems in magnesium

Slip system	Number of slip system	Number of independent slip system
Basal <a>	3	2
Prismatic <a>	3	2
Pyramidal <a> type I	6	4
Pyramidal <c+a> type II	6	2

The two common forms of function f involve either an L^1or an L^2 norm which are defined as [21, 22]:

$$\boldsymbol{L^1 = \sum_{t=1}^{N} \left| \rho_{gnd}^{t} W^t \right|} \quad \textbf{1-5}$$

$$\boldsymbol{L^2 = \left[\sum_{t=1}^{N} \left[\rho_{gnd}^{t} W^t \right]^2 \right]^{\frac{1}{2}}} \quad \textbf{1-6}$$

where the quantity W^t is an appropriate weight factor for ρ_{gnd}^{t}. The idea is to minimize $L^1$and L^2 for a set of suitable W^t. The L^2 norm does not have a fundamental physical interpretation, but may be more convenient to solve numerically [23]. In the case of the L^1norm, one choice for W^t is the line energy of individual dislocation type; and if the line energy is isotropic and all dislocation types have the same line energy, the weights for all slip systems are identical and the total dislocation density is minimized [21, 24, 25]:

$$\boldsymbol{\rho_{gnd} = \sum_{t=1}^{N} \rho^t} \quad \textbf{1-7}$$

A second option for weights is to use the magnitude of the relevant Burger's vector, b^t. Alternatively, in order to minimize the elastic energy present in the dislocation core, one might set $W = \mu \times (\, b^t)^2$ where μ is the relevant elastic shear modulus [23].

Another option for the weights is to consider the critical resolved shear stress (CRSS) for the relevant slip system. For example, in Mg the weight might be the CRSS for a slip system compared with that of basal slip, $W^t = \tau_{CRSS}^t / \tau_{CRSS}^{basal}$. If the macro-scale deformation strain is known, this might also be included in the weights by determining a Schmid factor,S^t, for the relevant slip systems. Then we might define weights by: $W^t = 1 - S^t$. One may also use combinations of these approaches, as is applied in this study:

$$\boldsymbol{f = \sum_{t=1}^{N} (1 - S^t) * \frac{\tau_{CRSS}^t}{\tau_{CRSS}^{basal}} * \rho^t} \qquad \textbf{1-8}$$

1.3 Results

Two random small areas were chosen to study the relative activity of the basal, prismatic, and pyramidal slip systems at small strain of 0.5%. The IPF maps of the grains are shown in Fig. 1-2(a) and schematic unit lattice cells are superimposed on the maps to provide a better visual sense of the crystal orientations. The Schmid factor maps of <a> basal, <a> prismatic, <a> and <c+a> pyramidal slips were plotted in Fig. 1-2 (b-e) respectively. The CRSS were not considered in generating the Schmid factor maps; hence activity of different slip systems cannot be predicted solely by comparing the Schmid maps. For example a grain with the high Schmid in the prismatic map does not necessarily have a higher probability of prismatic activation since the CRSS is higher than the basal slip system. However, each map by itself can represent relative activities for that slip system type in different grains.

Figure 1-3 shows total dislocation density and resolved dislocation maps for $<11\bar{2}0>$ {0001} basal, $<11\bar{2}0>$ $\{10\bar{1}0\}$ prismatic, $<11\bar{2}0>$ $\{10\bar{1}1\}$ pyramidal, and $<11\bar{2}2>$ $\{10\bar{1}2\}$ pyramidal slip systems. In other ongoing research we have shown dependency of the measured dislocation density with scan step size [26]. Although the total and resolved dislocation densities are changed by step size, the ratios of resolved slip systems remain constant. Hence the magnitudes of the dislocation densities are not reported in this paper. In both scanned areas in Fig. 1-2, a slight increase in total dislocation density takes places even after 0.5% strain, and also different grain orientations and grain boundaries have different responses to the strain. As observed in the Fig. 1-3, the resolved dislocation density maps are in good agreement with Schmid factor levels for each slip system in each grain; for instance, in both areas the only two grains which have high Schmid factor for basal slip showed up with higher values in the <a> basal dislocation maps. Inasmuch as the material has highly basal texture, low <a>basal activity is detected in other grains, also for the same reason, negligible amounts of pyramidal <a> activity present in both areas. Furthermore, the pyramidal <a> slip map has a poor agreement with the associated Schmid factor; i.e on both areas, the grains with the highest Schmid factor for pyramidal <a> system don't show any activity after 0.5% strain; while in each area a grain with intermediate Schmid factor shows some pyramidal <a> activities after 0.5% strain. Low activity of pyramidal <a> slip system is in agreement with previous experimental and simulated researches in which basal<a>, prismatic <a>, and pyramidal <c+a> were only observed or predicted [4, 5, 12, 14, 16]. The absence of pyramidal <a> slip system might relate to high CRSS value for this type of dislocation. Although the possibility of presence of this type of slip system is undeniable, if the orientation evolution caused by that slip systems is less than noise threshold the activity of that type would be ignored. The noise threshold could be as a result of step size selection. One

possibility is to combine all <a> slip systems into one map and compare that with <c+a> pyramidal slip system. In this regards, slip systems with different magnitude of burgers vector, <a> and <c+a> types, are investigated in further maps.

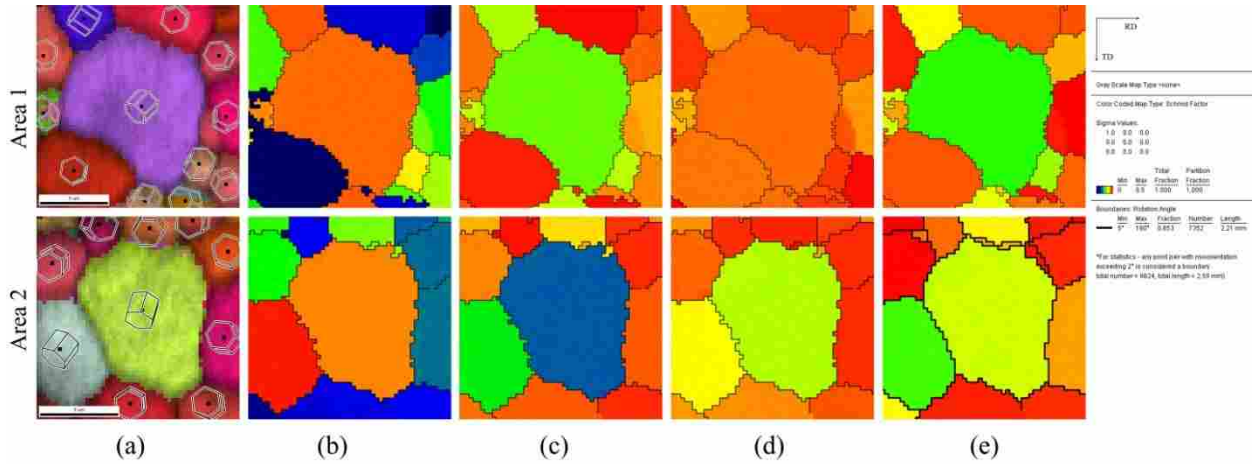

Figure 1-2. (a) Inverse pole figure maps,IPF, and related Schmid factor maps for (b) <11$\bar{2}$0> (0001) basal, (c) <11$\bar{2}$0> {10$\bar{1}$0} prismatic, (d) <11$\bar{2}$0> {10$\bar{1}$1} pyramidal, and (e) <11$\bar{2}$2> {10$\bar{1}$2} pyramidal slip systems. Based on the key bar next to the maps, the more reddish color represents the higher Schmid factor.

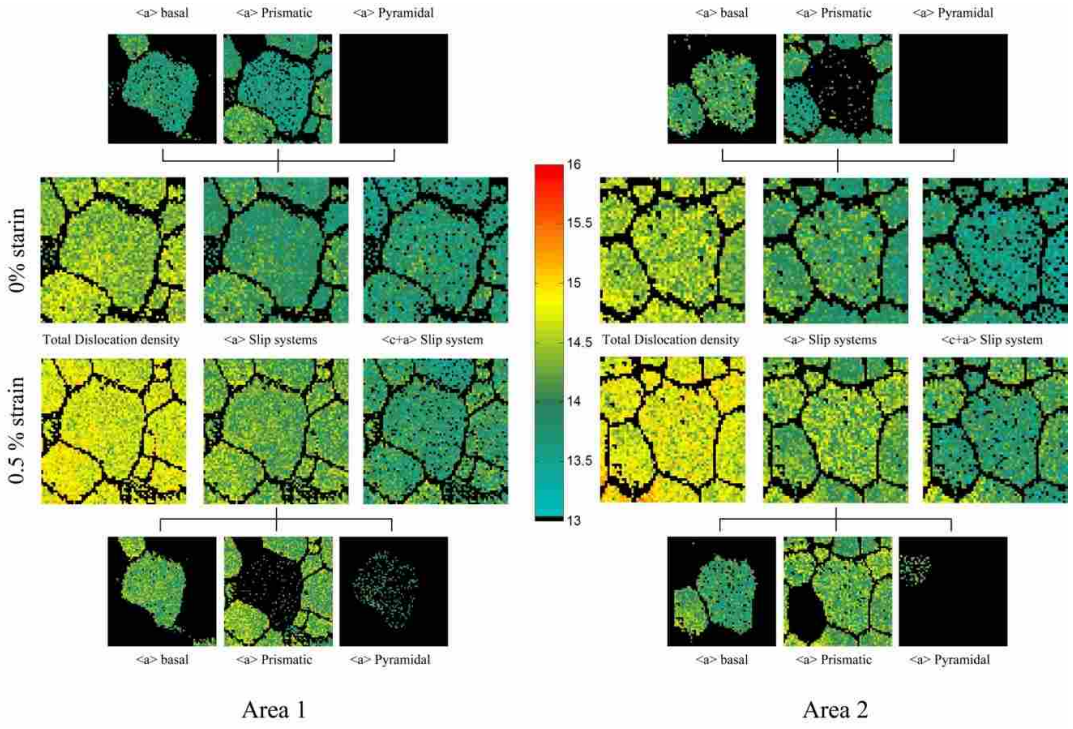

Figure 1-3. Total dislocation density's and resolved slip systems maps of area 1and 2 for 0% and 0.5% strain.

Figure 1-4(a) shows a wider view of the microstructure of the undeformed material with intense basal texture, in which the c-axes of most of the grains are aligned parallel to the ND direction. The (0001) pole figure contours are spread more towards the RD than TD. The $\{10\bar{1}0\}$ pole figure indicates no preferred orientation for prismatic and pyramidal planes, and a-axes of the HCP lattice are randomly oriented in the rolling plane. Figure 1-4(b) shows the inverse pole figure (IPF) map after 2.5% compression strain along TD. Compression along TD will cause expansion along the ND / c-axes, which is favorable for tensile twin formation. The tensile twins re-orient the lattice by 86° toward the load direction which is evident from diminished basal texture and appearance of the component in the transverse direction on the (0001) pole figure.

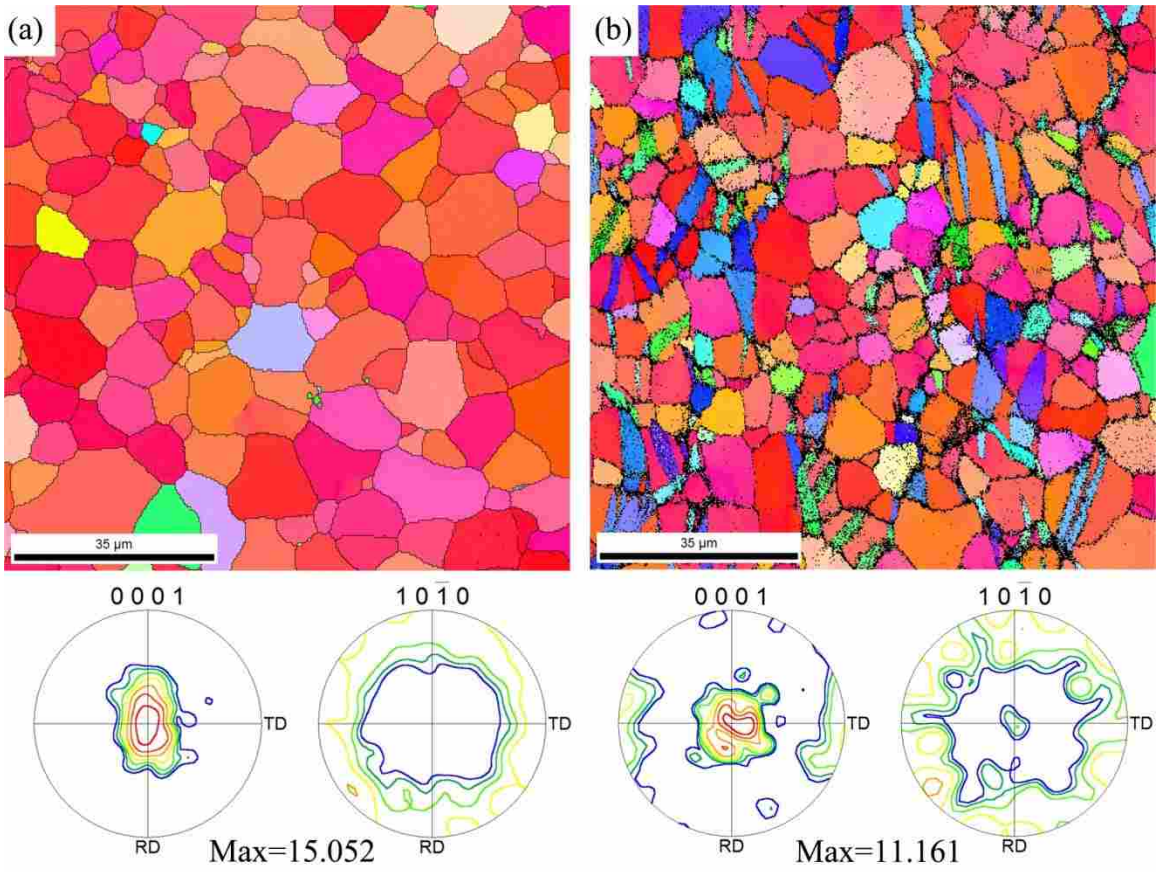

Figure 1-4. IPF maps and associated (0001) and $\{10\bar{1}0\}$ pole figures of (a) undeformed and (b) 2.5% deformation AZ31 magnesium alloy.

Figure 1-5(a) and 1-5(b) show different boundary types in terms of misorientation on Image quality (IQ) maps of undeformed and 2.5% strain respectively. In undeformed sample almost 60% of the boundaries' misorientations are in the range of 13.2 to 39° and 18.6% in the range of 39-53°while after 2.5% strain 31 % of the boundaries have misorientation of 80-90° which correspond to tensile twin's boundaries.

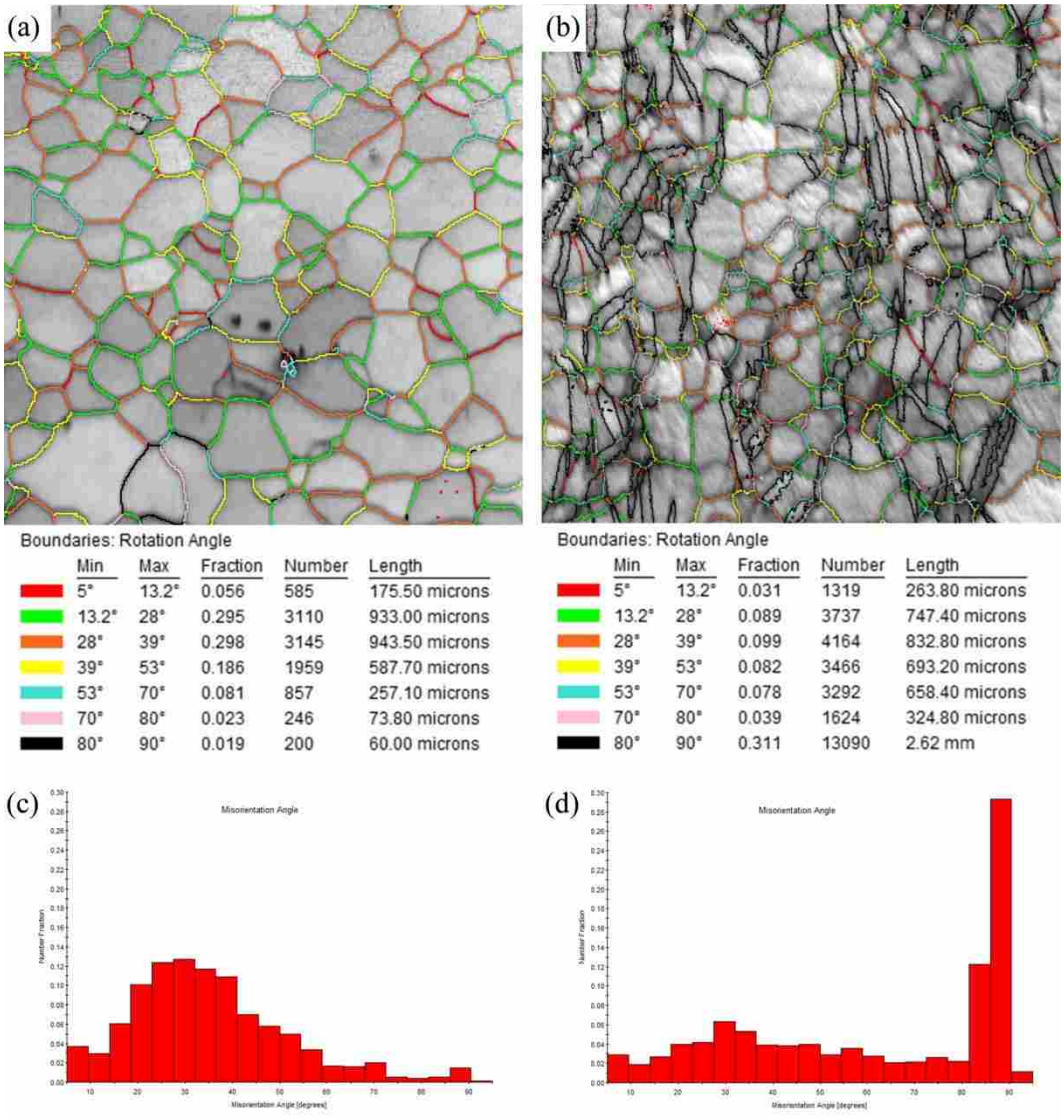

Figure 1-5. Grain boundaries on IQ maps showing different misorientations for undeformed (a) and deformed (b) material, and related distributions of misorientation angle (c and d).

Experimental detection of twin nuclei by EBSD is limited by the scan step size and poor IQ at the grain boundaries. It may happen that noise in highly deformed regions is confused for a twin, or a twin nucleus is overlooked as a result of choosing too large of a step size or due to low image quality. Compressing the Mg samples by 2.5% strain causes tensile twins to form copiously across the microstructure, but at this strain level, twin thickening is not prevalent, and numbers of untwined grains can be found. In the case of Fig. 1-5(b), 17% of the total scan area is twinned. Since at 2.5% strain twinning has not been developed in all grains, it is possible to find some grains in which a tensile twin is spontaneously formed at a grain boundary or nucleation may be caused by another twin in a neighboring grain. In the rest of the paper these two nucleation types are referred to as slip-assisted and twin-assisted respectively. Figure 1-6 show three tensile twins which appear to have formed independently at grain boundaries or triple junctions and have not passed through the parent grain. Each figure includes a total dislocation density map, <a> and <c+a> slip systems maps, and a boundary misorientation map.

As one can see in Fig. 1-6 more than one twin can nucleate in any given grain at this deformation level. For instance in regions 2 and 3 multiple twins have started nucleating, as indicated by T_1, T_2, T_3 and T_4 in the figures. The grain boundary misorientations wherein twins nucleated all fall into the range of high angle boundaries. Figure 1-7 shows distribution of misorientation angle for 93 cases in which twinning happened spontaneously at grain boundaries. Slip-assisted twinning is more likely to nucleate at the grain boundaries with miorientation angle of 35-45°. The Total dislocation density map shows higher activity of slip systems close to these kinds of boundaries including twin boundaries. Resolved dislocation maps show more <a> slip contents in the vicinity of the high angle boundary in the grains labeled with a ‘g’ (the grains

neighboring the twinning nucleation site), and also less <c+a> content is observed. Moreover, the twinned regions have lower dislocation densities than parent grains. The split dislocation maps reveal that less total dislocation activity inside the twins is the result of less <c+a> slip content rather than <a> slip type; this is more evident in region 3, which has a larger twin. The <a> slip map shows homogenous distribution inside and outside of the twin.

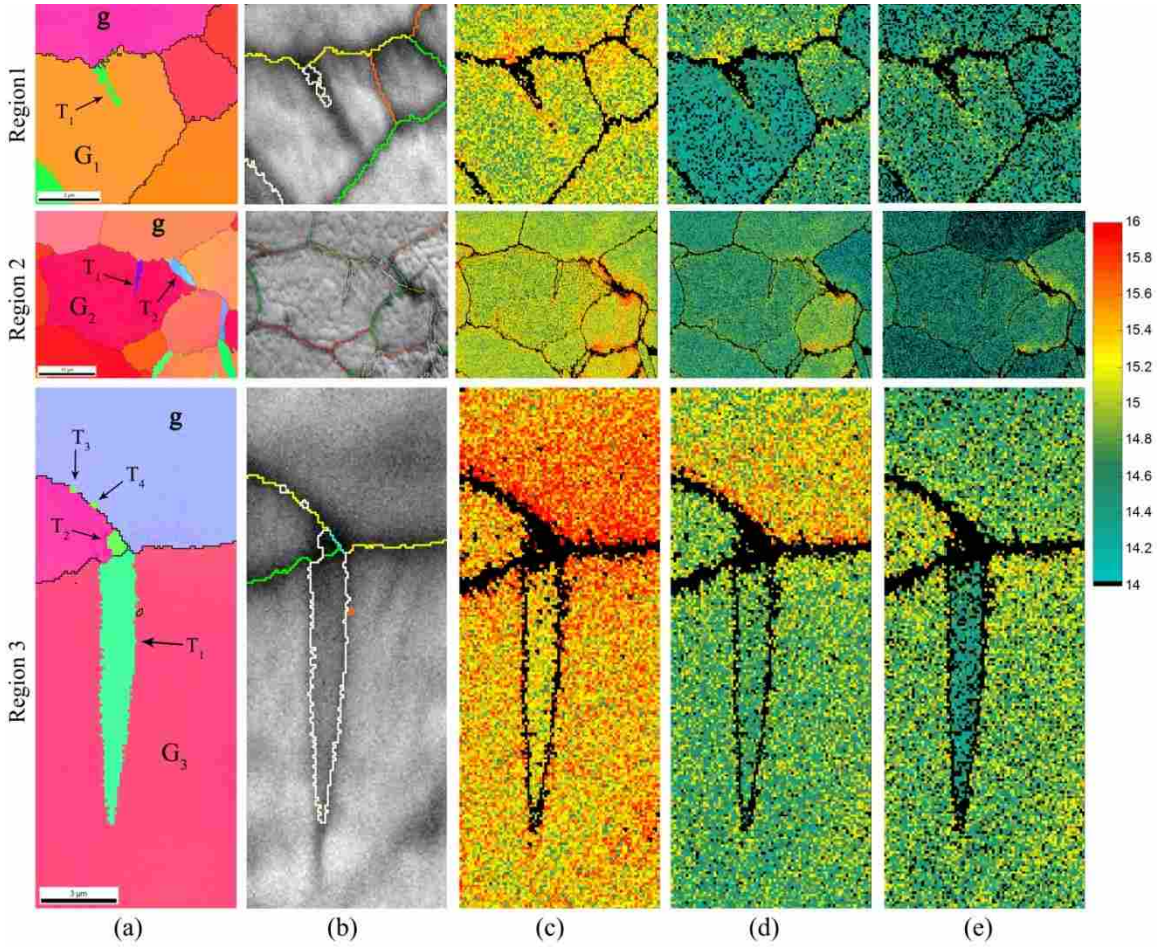

Figure 1-6. IPF (a), IQ (b), and dislocation density maps ((c) total GND, (d) <a>-type, (e) <c+a>-type) of the grains with the self nucleated twins. See Fig. 1-5 for the key to misorientation levels; the dislocation density level is a log scale.

Knowing the orientation of each grain, as well as the loading direction, permits the calculation of Schmid factors pertaining to the six possible $\{10\bar{1}2\}$ twin variants:$(10\bar{1}2)[\bar{1}011]$, $(01\bar{1}2)[0\bar{1}11]$, $(\bar{1}102)[1\bar{1}01]$, $(\bar{1}012)[10\bar{1}1]$, $(0\bar{1}12)[01\bar{1}1]$, and $(1\bar{1}02)[\bar{1}101]$. Theoretically, tensile $\{10\bar{1}2\}$ twin can be formed in six equivalent planes, with a specific shear direction. Twinning differs from slip activity by its polar nature; i.e. twins form in just one direction in the twin plane. Hence a shear vector is considered in the Schmid formula instead of a shear line; this leads to a negative Schmid factor for some of the twin variants. In other words, the twin variant with negative Schmid factor has no chance of being formed in the parent grain, even if it has a high absolute Schmid factor. In Fig. 1-8, the orientation of each of the G1, G2, and G3 grains shown in Fig. 1-6 are indicated in (0001) pole figures. The orientation of six possible twin variants with corresponding Schmid factors are plotted in the pole figure. The arrows indicate the twin variant formed during experiment. It is evident that twin variant selection obeys the Schmid factor; however twins with lower Schmid factors still have a possibility of nucleating.

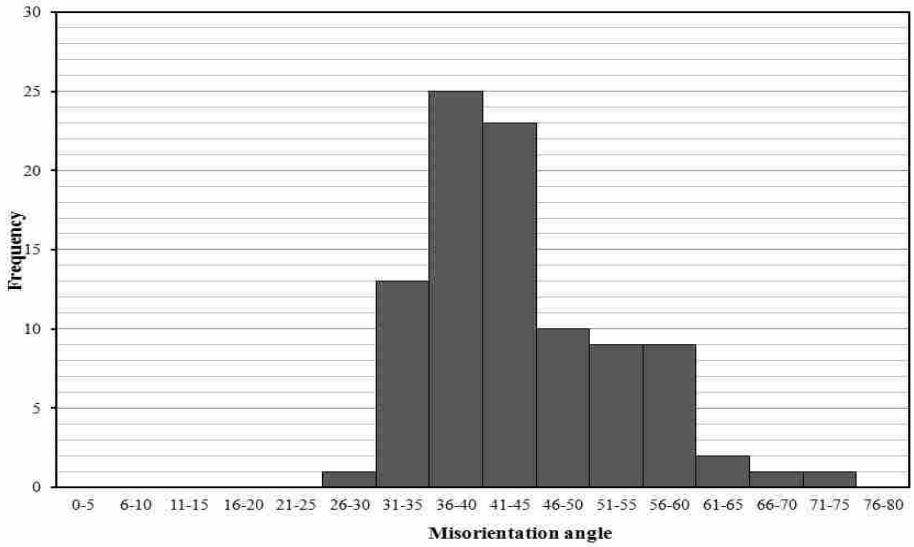

Figure 1-7. Misorientation angle distribution of the boundaries at which slip-assisted twinning formed.

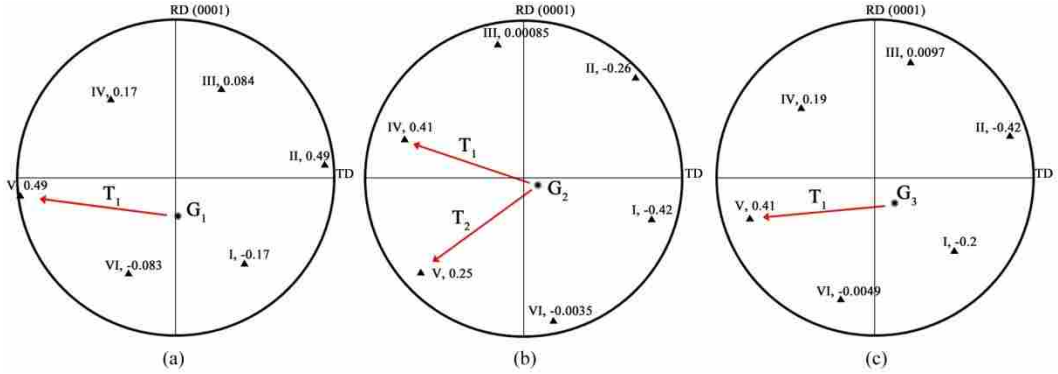

Figure 1-8. The orientation location of G1 (a), G2 (b), and G3(c) grains in Fig. 1-6 and their corresponding six possible twin variants in (0001) pole figures. The experimental twin variant indicated by arrow and the Schmid factor value of each variant show twin nucleation obey Schmid factor law.

The formation of a twin leads to shear in the grain, and when the twin grows and intersects grain boundaries, it could cause twin nucleation in another grain. To investigate which paths twins choose to propagate along in the microstructure, several scans were taken at the area where twins transmit from one grain to another one. Three of these scans are shown in Fig. 1-9; as one can see, twin growth in one grain can result in twinning in neighboring grains; however, as it is evident, twins appear to transmit from one grain into another one through certain types of boundary. The higher angle grain boundaries (highlighted in yellow) don't allow twins to pass through (for example, see the region labeled by 'gb1' in region 1); these boundaries have high misorientation. In contrast, a twin can cause twinning in the neighboring grain at which misorientation is low (for example, the boundaries labeled by gb2). Figure 1-10 (a) and (b) show distributions of misorientation angle of these two boundaries' type, transmitting and blocking boundaries respectively. It is evident from Fig. 1-10 that most of the boundaries which allow the twinning to pass through have misorientation angle in the range of 15-25° and the misorietation

angles for the boundaries which block twin propagation fall in the range of 45-55°. In the scans of Fig. 1-9 higher total dislocation content is found at the twin tips, which is mostly <a> type slip

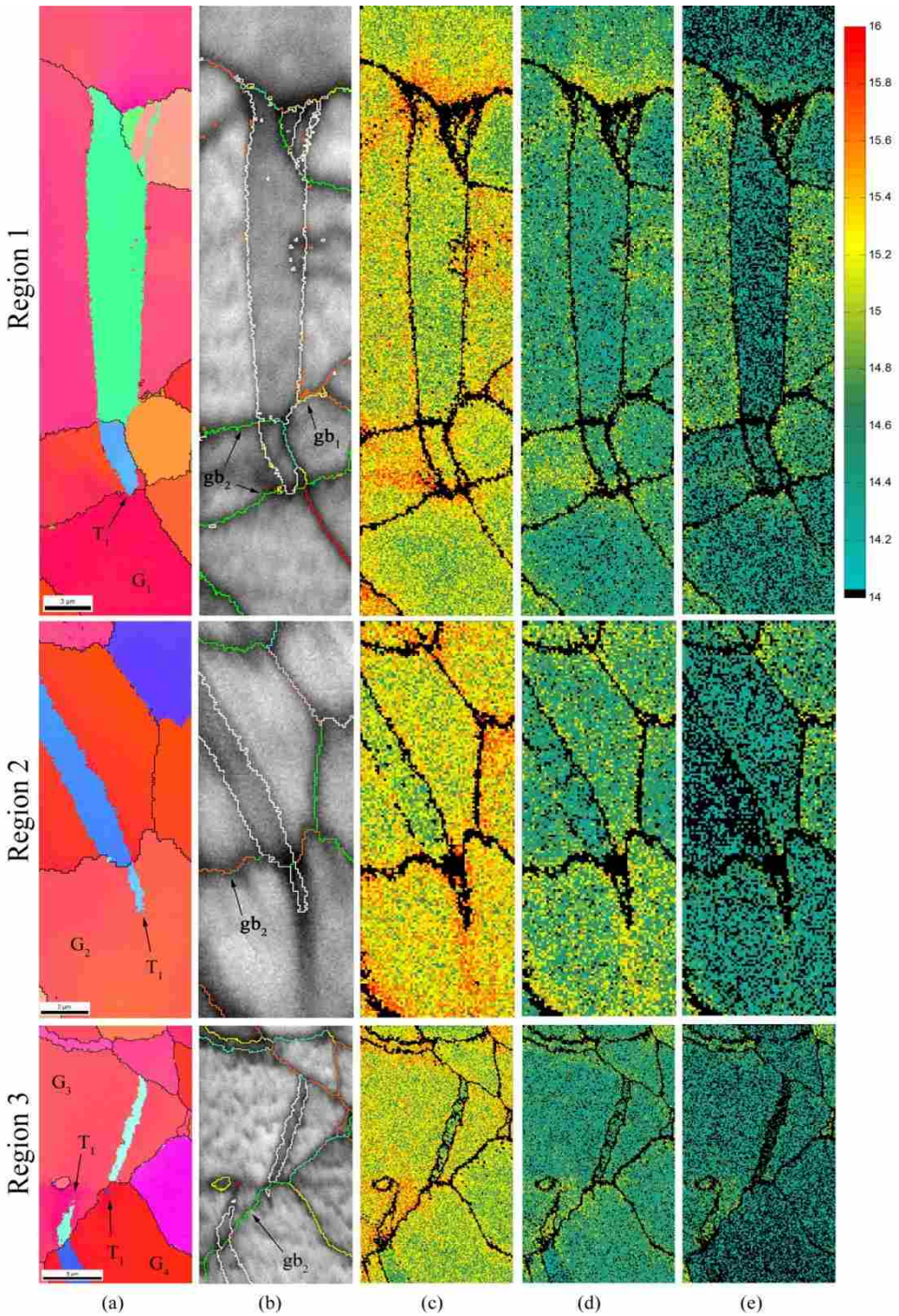

Figure 1-9. IPF (a), IQ (b), and dislocation density maps ((c) total GND, (d) <a>-type, (e) <c+a>-type) of the grains with the twin-assisted nucleation.

(notice the twins labeled by T1 and T2). Also except in the vicinity of the twin boundary in parent grain, type <a> slip maps show identical distribution inside and outside of the twins. It is more evident in large twins that <c+a> slip shows less activity inside the twinned regions; when the twin grows and consumes its parent; the twin appears to decrease <c+a> slip type in the grain while the <a> slip type remain unchanged. Figure 1-11 represents the area in which a twin is blocked at a grain boundary even up to 7% strain. The boundary indicated by an arrow has misorientation angle of 57°.

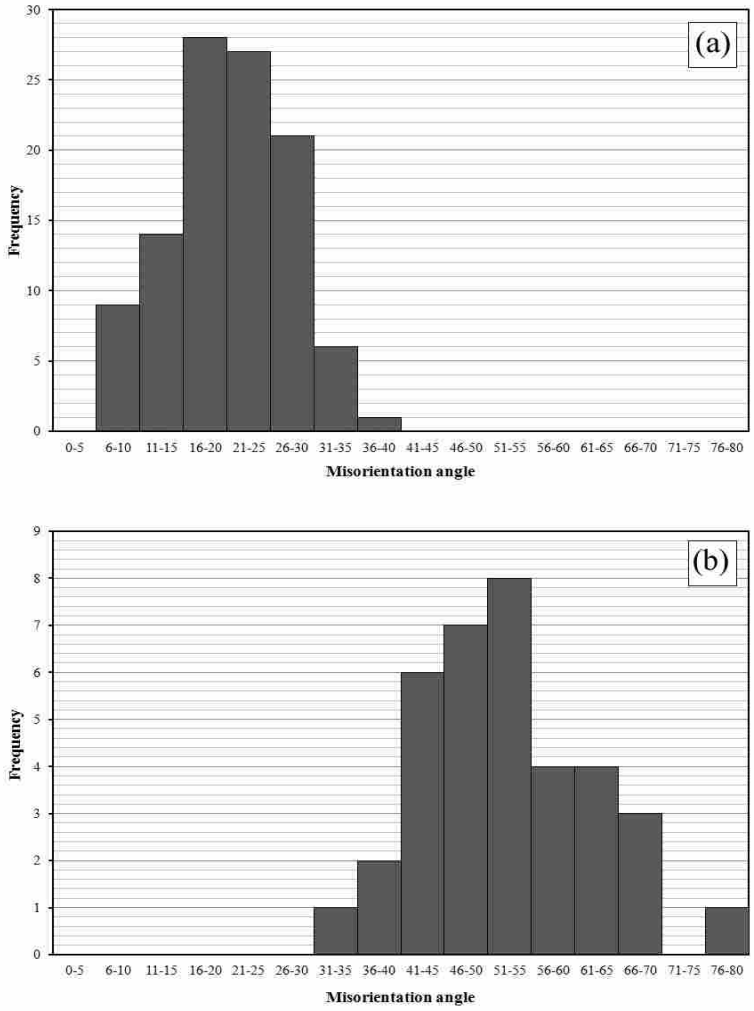

Figure 1-10. Misorientation angle distribution of the boundaries at which twin can propagated (a) and blocked (b)

The orientation of G1, G2, G3, and G4 grains in Fig. 1-9 are plotted in (0001) pole figures in Fig. 1-12 with the corresponding six possible twin variants in each grain. For this type of nucleation, which we call twin-assisted nucleation; twin variant selection still shows good agreement with Schmid factor.

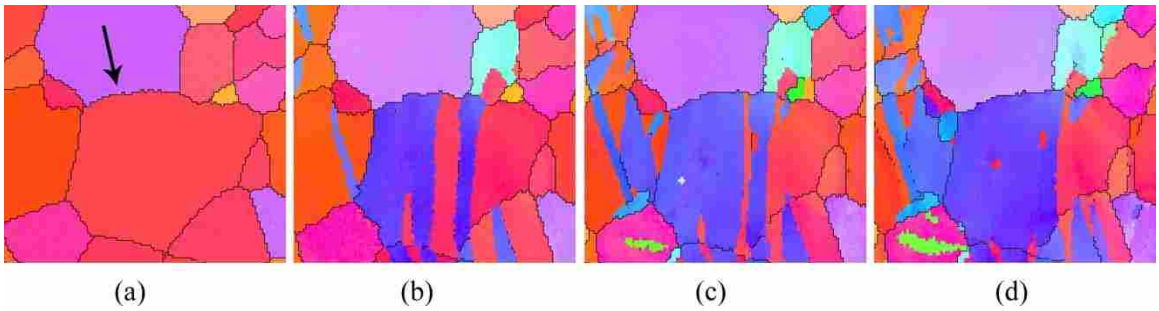

Figure 1-11. IPF map of small region during in-situ compression test at 1% (a), 3% (b), 5% (c), and 7% (d) strain showing a boundary, indicated by arrow, resist against twin propagation up to strain level of 7%.

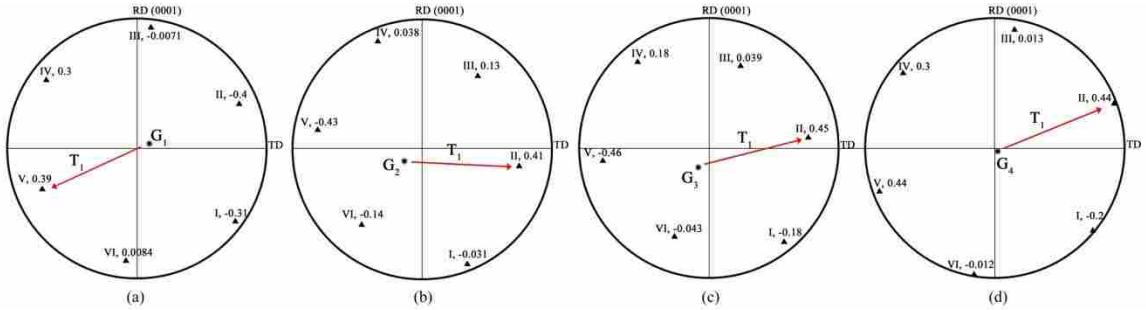

Figure 1-12. The orientation location of G1 (a), G2 (b), G3(c), and G4 (d) grains in Fig. 9 and their corresponding six possible twin variants in (0001) pole figures. The experimental twin variant indicated by arrow and the Schmid factor value of each variant show twin nucleation obey Schmid factor law.

Figure 1-13 shows a larger scan, including several grains in which twinning (nucleation and propagation to various extents) has occurred in some grains, but other grains are twin-free. In promising agreement with the previous observations, the twins pass through boundaries whose

misorientation is less than 40° but they are not able to transmit through high angle-misoriented boundaries (T1 twin in Fig. 1-13); however slip-assisted twins can form at the higher angle boundaries (T2 twins in Fig. 1-13). The total dislocation map shows more activity of slip systems at grain boundaries as well as at twin boundaries. As it can be seen in the <a> and <c+a> dislocation maps, the grains with twins have less <c+a> slip contents but more <a> type.

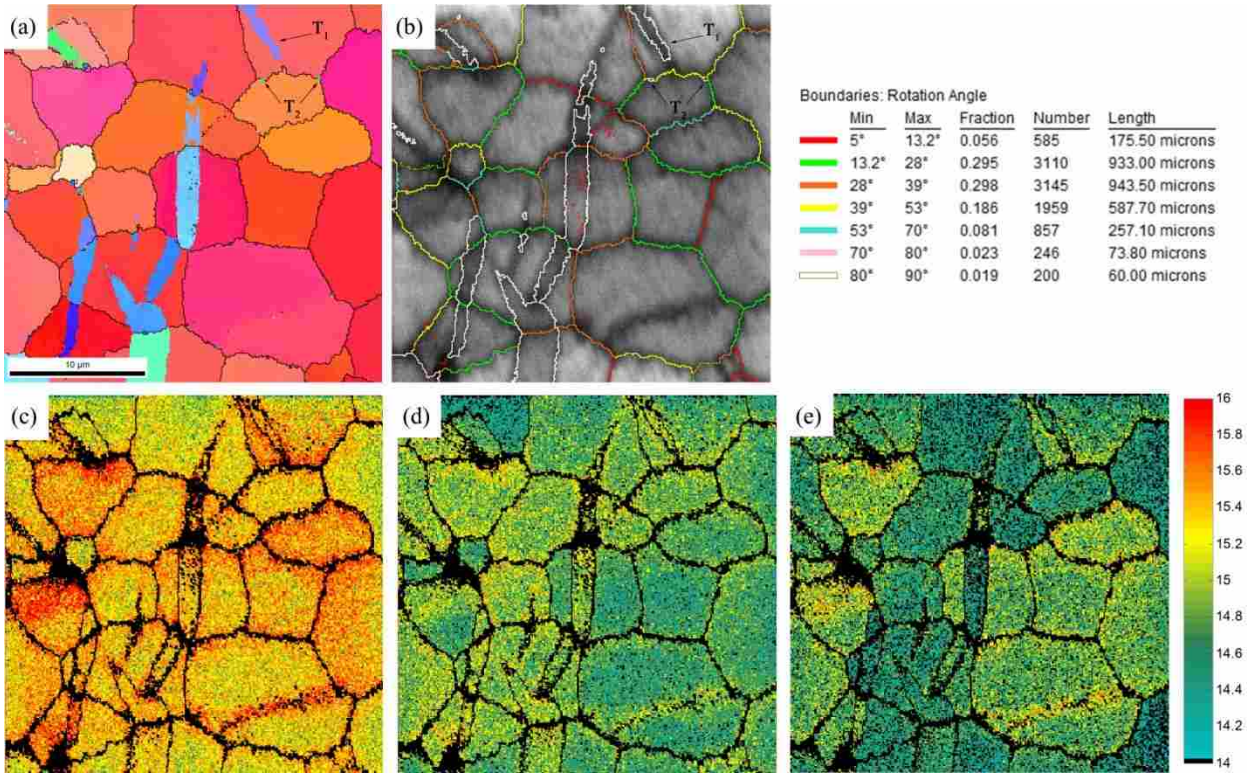

Figure 1-13. IPF (a), IQ (b), and dislocation density maps ((c) total GND, (d) <a>-type, (e) <c+a>-type) of the area in which the twins propagate through some of the grains.

1.4 Discussions

In this investigation we have used HR-EBSD techniques to study tensile twin nucleation in AZ31 Mg. The twin nucleation appears to relate to dislocation pile-up at neighboring grain in two ways: (a) twin nucleation which is the result of <a> slip type accumulation behind the high

angle-misoriented boundary (slip-assisted twinning) and (b) nucleation which is the result of dislocation pile up at the tip of a twin intersecting low angle-grain boundaries (twin-assisted twinning).

1.4.1 Total and resolved dislocation densities

The evolution of dislocations maps in Fig. 1-3 shows activation of slip systems at low strain level of 0.5 %. Once the deformation starts, dislocation sources increase the dislocation contents in the microstructure. Depending on boundary type, grain boundaries can act as a source for dislocation as well as a sink [27]. As is evident from Fig. 1-3, more dislocation content is observed at grain boundaries.

Dislocation content in grains was compared with Schmid factors on the available slip systems. In the Schmid factor calculation we assumed that the local stress state was identical to the global one, which is only an approximation to reality. However, the resolved dislocation maps show good agreement with Schmid factor maps. Although the CRSS for <a> basal slip is the lowest relative to other slip systems [4, 5, 8, 13, 14, 16], less activition of <a> basal slip is observed in the two small scans compared with <a> prismatic slip. This is the result of a strong basal texture of the material in which most of the grains are oriented in a more favorable direction for prismatic slip rather than basal. The <a> Pyramidal slip type shows negligible levels in both scan areas even though it has relatively high Schmid factor; the same result is observed after 2.5 % strain in other scans. The high CRSS for <a> pyramidal slip system is clearly a convincing reason for this.

1.4.2 Correlation of twin nucleation sites with <a> slip systems

As is evident in Fig. 1-6 and 1-9, the activities of <a> and <c+a> slip types differ for different grains based on their orientations. Once deformation starts, slip systems' activities in each grain are generally based on Schmid factor and CRSS values for that type of slip system. The movement of dislocations is based on the strain field around the dislocation core and the magnitude of the Burgers vector. Lattice defects, such as twin and grain boundaries, vacancies, and stacking faults, can promote or impede dislocation movement. The split dislocation maps in Fig. 1-6 and Fig. 1-9 show pile up of <a> slip type at high angle grain boundaries. The lattices of the grains at the two sides of these boundaries have strong mismatch, which makes it difficult for dislocations to glide from one grain to another one [27]. Therefore accumulation of the dislocation happens at these boundaries. As suggested by Koike[5], to accommodate incompatibility stress caused by basal slip systems at grain boundaries and to avoid grain separation, <c+a> slip systems are required. Twinning is the alternative option for stress accommodation. From this point of view, nucleation of the tensile twins is not surprising. In contrast, less <a> slip system pile up happens at low angle boundaries, therefore tensile twins have less chance for nucleation at those boundaries.

Once twins are formed, their boundaries also act as a barrier for dislocation movement. Yoo[28] reported that twin interfaces act as barriers to basal dislocations. As it is evident in the split dislocation maps, higher <a> and <c+a> slip activity can be observed at twin boundaries and twin tips. Upon further deformation, twin growth continues until it reaches the other side of the parent grain. Depending on the boundary type that it then encounters, twins can transmit to neighboring grain or be suppressed. As it is shown in Fig. 1-9, if the grain boundary has low angle misorientation, 15-25°, the <a> slip pile up at the twin tip can transmit to the neighboring

grain and cause twinning in the neighboring grain. In contrast to this mechanism, if the twin reaches a high angle boundary, 45-55°, the <a> slip content at the twin tip is not enough to shear the neighboring grain. Therefore at the observed strain level the twin is impeded by high angle boundaries. Further deformation may provide sufficient localized slip activity to transmit the twin to another grain.

Huber and Hatherly [29, 30] in their studies on brass showed that twins can relax accumulated strain due to heavy cold-rolling. They called these twins 'recovery twins' and they showed that dislocation density inside the twins is lower than outside of the twins. The result from considering relative dislocation activity in Fig. 1-6, Fig. 1-9, and Fig. 1-13 shows lower dislocation content inside the twin as a result of less <c+a> slip type inside the twin.

The twin variant selection is studied in relation to Schmid factor in some grains in Fig. 1-6 and Fig. 1-9. Since the texture is a highly basal one, having a high Schmid factor of 0.45 for at least one of the twin variant is not surprising. Figure 1-8 and 1-11 show that tensile twinning is governed by Schmid factor. In other word, tensile twinning due to a strain path of compression along TD obeys the Schmid factor criterion. However, the twins with lower Schmid factor still have the chance be nucleated.

1.4.3 Deformation mechanisms: twinning vs <c+a> pyramidal slip system

In magnesium alloy because of limited numbers of independent basal slip systems, some other type of deformation accommodation is required to satisfy von-Mises criterion. <c+a> pyramidal slip system and twinning potentially play an important role in magnesium deformation since they provide mechanisms which can accommodate strain along the c-axis in HCP crystals. Nucleation of tensile twins typically correspond with a lower CRSS than that required for

activation of <c+a> pyramidal slip sytems at room temperature [6]. Nevertheless, it is postulated that at the small strain levels present in the samples of this study tensile twins are predominantly nucleated at high angle grain boundaries. The misorientation distribution map in Fig. 1-5(c) shows that only 30% of the boundaries in the undeformed material have misorientation above 39°. In addition, because of basal texture of the material, the Schmid factors for basal slip for most of the grain are low. In other words, two of the factors which promote slip-assisted twinning are absent in many of the grains. Relatively higher amounts of <c+a> pyramidal slip may then be expected in twin-free grains. Relative dislocation activity maps in Fig. 1-13 shows higher amounts of <c+a> slip contents in the twin-free grains. Those grains have low activity of <a> slip systems or have high-angle grain boundaries which makes them unfavorable for twin nucleation and propagation. Strain accommodation along the c-axis in these grain is partially satisfied by activation of <c+a> slip systems. In contrast, in the grains contain tensile twin, strain along the c-axis is provided by twins and the <c+a>slip system is not required to be activated.

1.5 Conclusions

The aim of this study was to investigate correlations relating to tensile twin nucleation / propagation using HR-EBSD techniques. Using this approach, total and resolved dislocation densities can be derived from the EBSPs (electron backscattered patterns). The main results can be summarized as follows:

1. Tensile twinning strongly obeys a Schmid factor criterion. The twin variant with higher Schmid factor is activated; meanwhile the twin variant with second rank Schmid factor has a chance to form in the grain.

2. Tensile twin nucleation predominantly occurs in a grain which meets two requirements: the grain has a boundary with misorientation of higher than 39° and high activity of <a> slip systems present on the other side of that boundary in a neighboring grain.
3. Tensile twinning and pyramidal <c+a> slip systems compete for strain accommodation along the c-axis. In a grain which has low chance of twinning, higher activity of <c+a> pyramidal slip is present.
4. At low strain, high-angle grain boundaries, in the range of 45-55° don't allow twins to transmit through them to the other grain and cause twinning in neighboring grain. In other word, the dislocation pile up at the twin tip is not enough to shear the adjacent grain at high-angle grain boundaries. In contrast, tensile twins can propagate through low angle grain boundaries (15-25° misorientation); at these boundaries dislocation pile up at a twin tip can produce incompatibility stress at the grain boundary which leads to formation of another twin in the neighboring grain. The tensile twins can be considered as recovery twins in the AZ31 magnesium alloy, causing strain relaxation by diminishing <c+a> slip content inside the twin.

2 IN-SITU MICROSTRUCTURE EVOLUTION OF AZ31 MG ALLOY AT DIFFERENT STRAIN PATHS

Abstract

Microstructure evolution of AZ31 magnesium alloy was investigated during in-situ compression and tension tests by means of high-resolution electron backscatter diffraction (HR-EBSD) techniques which provide information on geometrically necessary dislocations (GND) from the scanned area. Compression and tension tests were performed at room temperature to various strain level up to 7% strain. The results show twin formation and total dislocation density strongly depends on initial microstructure and load directions. In the rolled sheet with deviation away from basal texture spreading along the rolling direction (RD) in the (0001) pole figure, twinning starts at lower strains when the sample is loaded along the transverse direction (TD). On the other hand, total dislocation density increases more rapidly when the sample is loaded along the rolling direction.

2.1 Introduction

Application of magnesium alloys has been increased substantially in automotive, aircraft, and electronic industries because of specific properties of the Mg alloys. In the last few decades, in order to reduce vehicle weight, many efforts have been made to accelerate its adoption. Replacement of heavy components of the automobile with Mg improves fuel efficiency and reduces the harmful gas emissions [2, 4, 6-8, 15, 31, 32]. Magnesium and its alloys are the

lightest structural metals, providing good mechanical properties and the highest available strength over weight ratios in metal components [2, 32]. Wrought magnesium alloy products provide excellent mechanical properties[4, 5]; however, the casting process requires techniques which provides fine-grain microstructure, for example die-casting or Thixo-casting techniques, which are limited by solidification speed and processing cost [4, 5]. Furthermore, wrought magnesium alloys exhibit strong anisotropies and asymmetries in mechanical properties because of strong crystallographic texture and the intrinsic anisotropy in the HCP lattice [7, 8, 16, 32].

Wrought alloys are also unsuitable for many components, such as body panels in automotives. However, sheet material presents other issues. Room (or near-room) temperature forming of magnesium alloys is desirable to reduce energy and lubricant costs; but, formability of Mg alloys at ambient temperature is poor since the HCP lattice doesn't provide a sufficient number of active slip systems [2-7]. According to the von Mises' criterion, five independent slip systems are required for plastic deformation of polycrystalline materials, but popular alloys only have two active (basal), and two semi-active (prismatic) systems. Hence deformation twinning plays an important role in plastic deformation of magnesium alloys by adding additional active systems [3, 8-11].

It has been reported [8, 11, 33-35] that twin morphology, twin fraction, and texture may be changed by varying strain paths, leading to different mechanical behavior from previously identical materials. Hong et al [8] showed that tension along the normal direction (ND) of highly textured sheet will activate different twin variants in the grains, resulting in a random distribution of the c-axis for the twin texture in the RD-TD plane. In contrast they showed that compression along the RD results in activation of mostly one twin variant or a twin variant pair in all grains, and a preferred direction for the c-axis of the twin texture in the rolling direction; this helps basal

slip activity by increasing its corresponding Schmid factor. They concluded that the strain path can significantly affect flow stress and strain hardening. It has been seen [32, 35] that spreading of the sheet's basal texture toward RD or TD (in the (0001) pole figure) leads to lower flow stress if the sample is pulled along the direction of spread. This relates to the numbers of grains which are more favorably oriented for basal activity as well as for tensile twinning in the direction along which the basal texture spreads.

In this study, in-situ compression and tension tests were performed to investigate microstructure evolution for different load paths. The total dislocation densities at each strain levels were obtained using HR-EBSD techniques which provide deeper insights into the plastic deformation study of AZ31 magnesium alloy. For this purpose, a rolled AZ31 Mg sheet with an intense basal texture was used. The samples were loaded along the rolling direction (RD) and the transverse direction (TD) in compression and tension.

2.2 Experimental procedure

AZ31B magnesium sheet was annealed at 350 °C for 1 hour prior to in-situ tension and compression tests. Both the rolling and the transverse directions (RD and TD) of the sheet were aligned along the major strain axis. Compression cubes and tensile bars were machined from the homogenized plate by using wire EDM to avoid any residual stress during cutting; then the sample was mounted in cold resin and polished for EBSD scan preparation. The sample preparation procedure was grinding with 1200 grid SiC paper, polishing with 6, 3, and 1 μm oil-based diamond suspension, followed by OP-S colloidal silica slurry which provides high quality surface finishing for EBSD. The sample was etched with a solution of 60% ethanol, 20% distilled water, 15% acetic acid and 5% nitric acid. Using a focused ion beam (FIB), Platinum

fiducial marks were deposited on the sample's surface to measure local strain in the scan area. Uniaxial true strains of 1, 3, 5, and 7 % were achieved.

Automatic EBSD scans were performed using the FEI-Helios NanoLab^{TM} 600i SEM equipped with OIM^{TM} data acquisition software and a high-speed Hikari^{TM} camera. In order to get dislocation maps, the EBSPs (electron backscattered patterns) were saved in bmp format for all the scan points and later they were post-processed. Regular square grid scans were used to examine $84 \times 84\ \mu m^2$ with a 300 nm step size. Using cross correlation technique, the perturbation of the orientation between neighboring scan points can be measured from their corresponding EBSPs from which lattice distortion between the can be measured. The dislocation density tensor can be described as second rank tensor, with components α_{ij}. Nye and Kröner defined the components of dislocation tensor in terms of the components of lattice distortion (β_{ij}) tensor as [18]:

$$\boldsymbol{\alpha} = \boldsymbol{\nabla} \times \boldsymbol{\beta} \qquad \textbf{2-1}$$

$$\boldsymbol{\alpha_{ij}} = \boldsymbol{\epsilon_{nmj}\beta_{in,m}} \qquad \textbf{2-2}$$

where ϵ_{klj} is the permutation tensor. Note that scans from the surface of the sample only provide lattice gradients in the plane of the surface, hence only 12 of the required 18 components of lattice distortion, and therefore 3 fully determined, and several partially determined, components of the dislocation tensor can be derived.

Texture evolution studies of the scanned region during in-situ loading were performed using TSL^{TM} OIM software, and for this purpose data with a confidence index < 0.07 were filtered out. In addition, twin fractions in each strain level were calculated by the software with a misorientation tolerance of ±2° for characterizing tensile twin boundaries at 86.3°. The twin

fractions are calculated based on the ratio of the area of the twinned region divided by the total scanned area.

2.3 Results and discussions

The Inverse pole figure (IPF) map of the undeformed AZ31 magnesium sheet in annealed condition are shown in Fig. 2-1, where the corresponding (0001) and $\{10\bar{1}0\}$ pole figures show strong basal texture and random distribution of prismatic and pyramidal planes. The basal texture is more spread in RD which has been reported to influence the yielding behavior of the sheet under different load paths [32, 35].

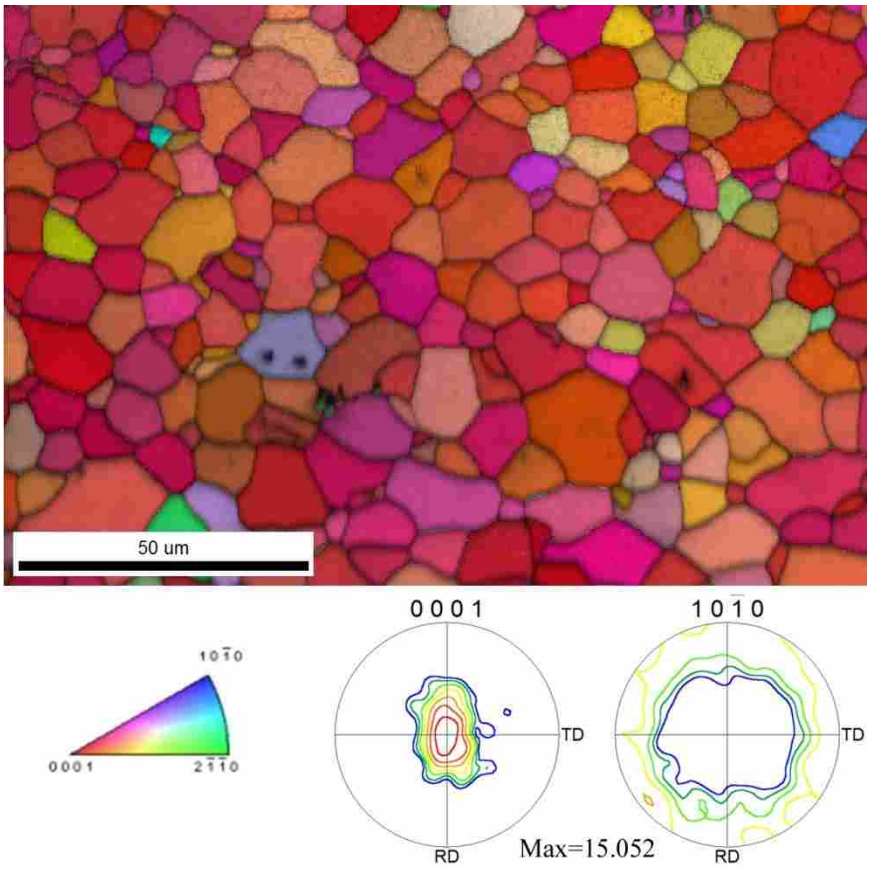

Figure 2-1. Inverse pole figure (IPF) map of undeformed sample in annealed condition and its corresponding (0001) and $\{10\bar{1}0\}$ pole figures.

2.3.1 In-situ compression tests

The microstructural evolutions of AZ31 Mg under different load paths are shown in Fig. 2-2. As is evident, massive fractions of twins are formed in compression tests relative to the tension tests (shown in the same figure). Compression of the AZ31 Mg sample along RD by 7% strain causes 25.4% of the scanned area to twin. The twin fraction for the sample compressed along TD is 23.5% for 5% strain. The plot in Fig. 2-3(a) shows that in the sample compressed along TD, the twin fractions at 1, 3, and 5% strain are higher than the corresponding levels for the sample compressed along RD at each strain level. In the sample compressed along TD, the scan of 7% strain was rejected due to the high level of noise in the scan, which was a result of poor diffracted patterns at that strain level. However, from the trend of twin fraction for previous strain levels, one would predict that the twin fraction at 7% strain for the C-TD (compression along TD) sample would be higher than C-RD (compression along RD).

The much higher twin fraction at 1% strain for the C-TD sample relative to the C-RD sample indicates that twin formation occurs at lower strain levels when the sample is compressed along the transverse direction as opposed to the rolling direction. This can also be inferred by looking at the initial (0001) pole figures of both regions in Fig. 2-4. The C-TD sample had an initial microstructure in which more basal planes were aligned with the normal direction of the sheet than C-RD sample. Hence, higher Schmid factor values for tensile twin variants are expected as shown in Fig. 2-5(a). Theoretically, tensile $\{10\bar{1}2\}$ twin can be formed in six equivalent planes, with a specific shear direction:$(10\bar{1}2)[\bar{1}011]$, $(01\bar{1}2)[0\bar{1}11]$, $(\bar{1}102)[1\bar{1}01]$, $(\bar{1}012)[10\bar{1}1]$, $(0\bar{1}12)[01\bar{1}1]$, and $(1\bar{1}02)[\bar{1}101]$. The Schmid factor is calculated using $SF = \cos\varphi \cos\gamma$. Twinning differs from slip activity by its polar nature; i.e. twins form in just one direction in the twin plane. Hence a shear vector is considered in the Schmid formula instead

of a shear line; this leads to a negative Schmid factor for some of the twin variants. In other words, the twin variant with negative Schmid factor has no chance of being formed in the parent grain, even if it has a high absolute Schmid factor. As it can be seen in Fig. 2-5(a) and Table 1, the C-TD sample not only has a slightly higher fraction of positive twin variants (81.7% vs 79.5%) but it also has a significantly higher average SF (0.403 vs 0.359) than the C-RD sample. These reasons help explain why twins in the C-TD sample formed at lower strain level than for the C-RD sample.

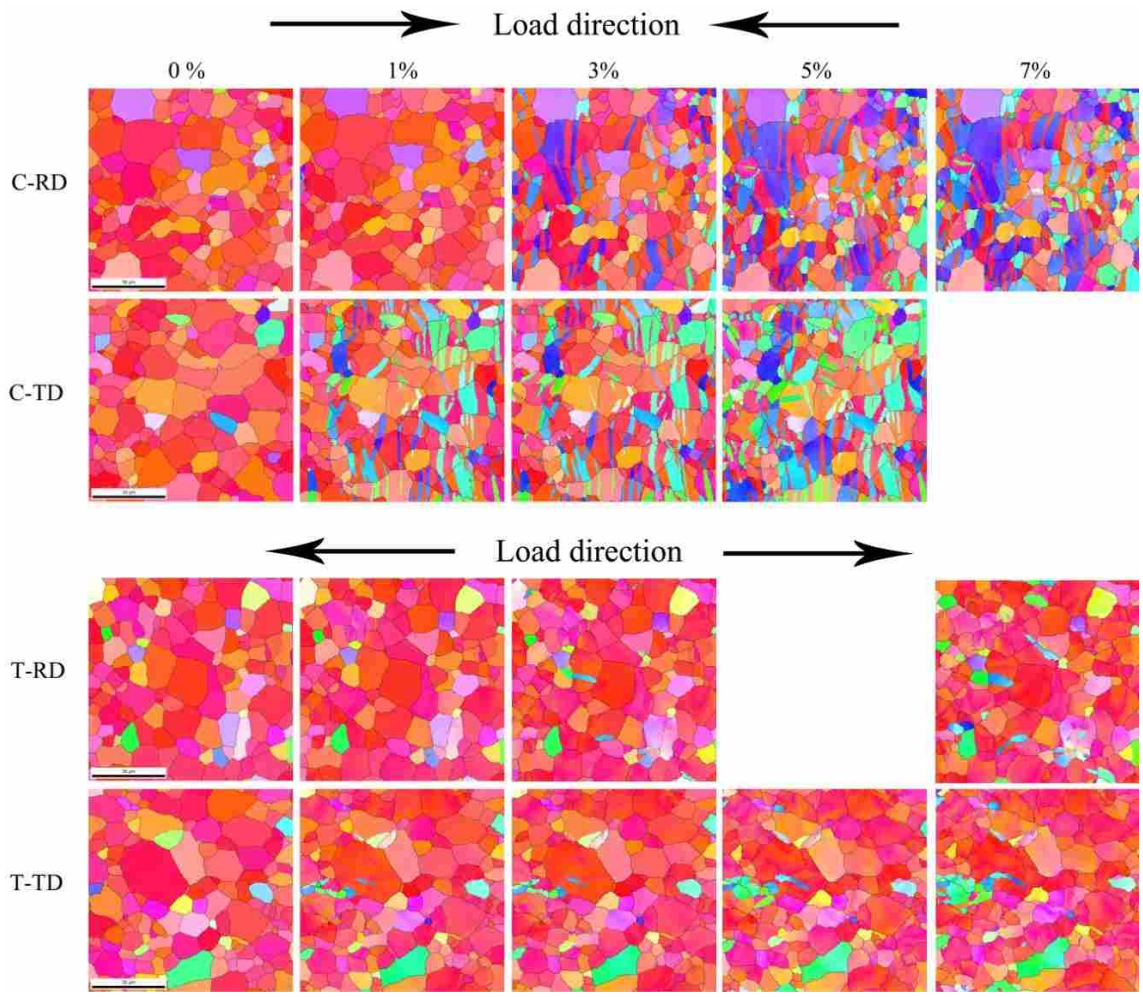

Figure 2-2. Inverse pole figure evolution of the AZ31 Mg strained along RD and TD during in-situ compression tests (C-RD and C-TD) and in-situ tension test (T-RD and T-TD) at several strain levels up to 7% (two missing subfigures are due to poor scans at these strain levels).

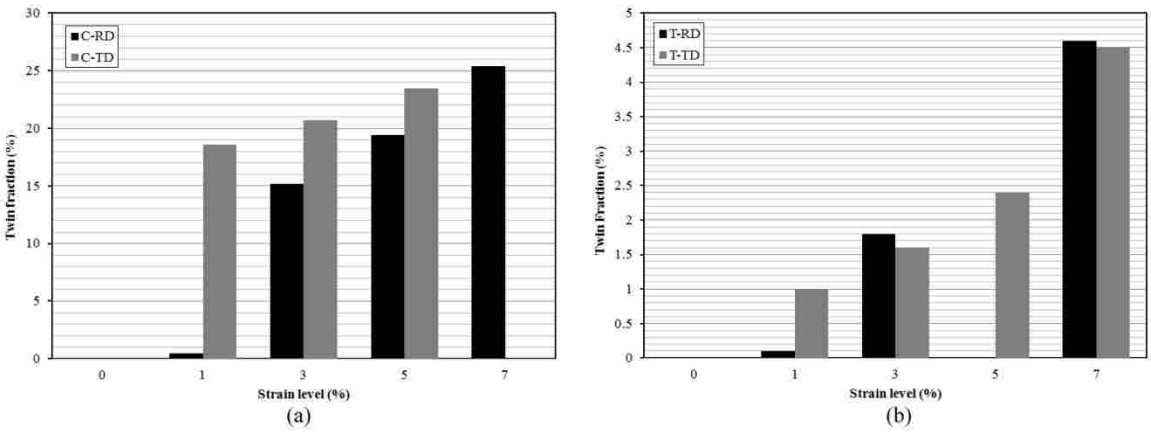

Figure 2-3. Twin fractions at different strain levels for in-situ compression tests (a) and in-situ tensile tests (b)

Total dislocation density maps of initial microstructure and final strained C-RD and C-TD sample are shown in Fig. 2-6. In other ongoing research we have shown dependency of the measured dislocation density with scan step size. Hence the reported magnitudes of the dislocation densities in Fig. 2-7 use a constant 300 nm step size for each scan. Although the initial dislocation density for C-RD sample is less than that for C-TD, the dislocation density increased much sharper in C-RD sample than in the C-TD sample. This may relate to the initial texture of the samples. As shown in Fig. 2-4, the basal texture for C-RD sample spreads more along the rolling direction, which makes the activation of the basal slip system easier by increasing the SF. The distribution of SF values of undeformed condition in the C-RD and C-TD samples were plotted in Fig. 2-8(a). As it is evident in the plot, the fraction of grain with higher Schmid factor for basal slip system is higher when the sample is loaded along rolling direction than transverse direction. The average Schmid factors for basal slip system in C-RD and C-TD samples are 0.306 and 0.274 respectively. The C-TD sample is less favorable for basal slip activity, and more favorable for twin formation at lower strain levels (as discussed above)

leading to higher twin fraction and lower GND content, since mechanical twinning and slip system activity are two competing deformation mechanisms in HCP materials. In both C-RD and C-TD samples total dislocation densities decrease after 5% and 3% strain respectively. This could be a result of twin formation and growth. It has been observed [29, 30] that dislocation density inside the twin region is less than in the parent grain (recovery twinning). Therefore by consuming parent grains with twins, total dislocation density of the sample decreases.

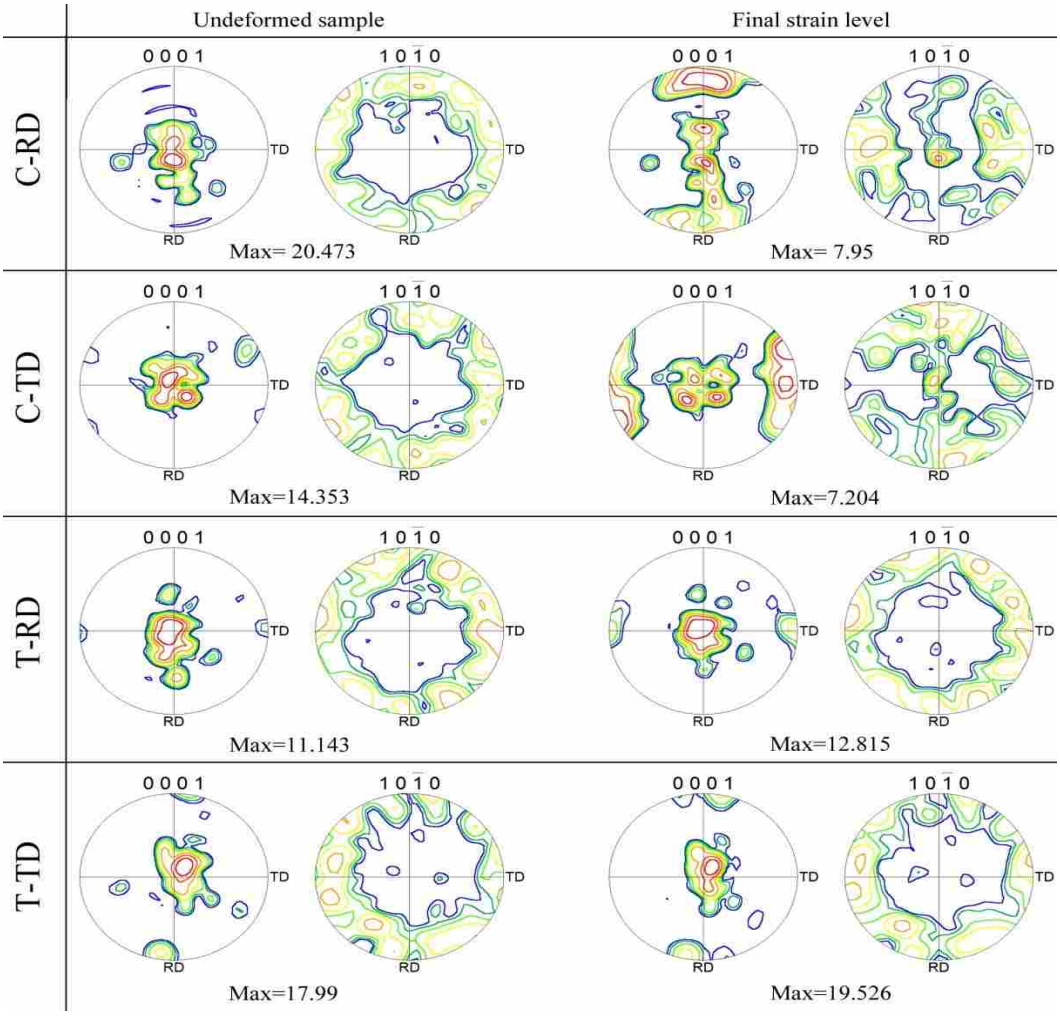

Figure 2-4. Initial and final (0001) and {$10\bar{1}0$} pole figures of the sample at different strain paths: Compression test along RD (C-RD), compression test along TD (C-TD), tension test along RD (T-RD), and tension test along TD (T-TD).

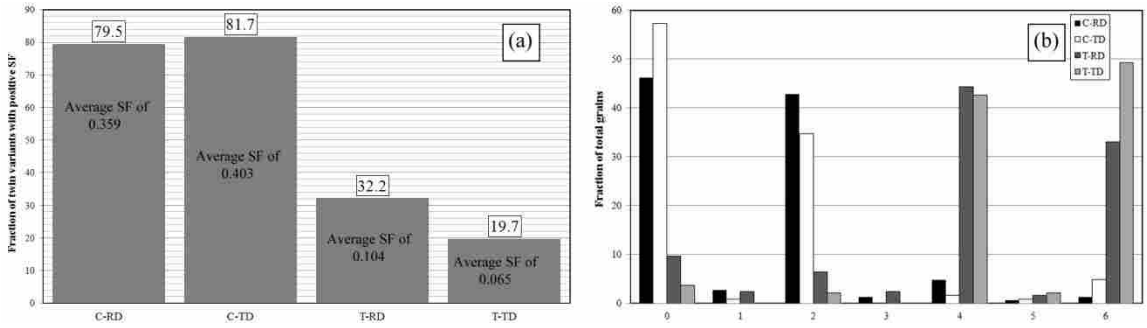

Figure 2-5. Fraction of twin variants with positive SF values in the scanned area, and the average of two highest ones at each grain at different strain paths (a), fraction of grain with 0, 1, 2, 3, 4, 5, and 6 twin variants with negative SF values for different strain paths (b).

Table 2-1. Statistical information of the scanned area in each in-situ test.

Sample	C-RD	C-TD	T-RD	T-TD
Numbers of grains in scanned area	147	124	124	136
Numbers of twin variants	882	744	744	816
Numbers of twin variants with positive SF	701	608	240	161
Fraction of twin variants with positive SF (%)	79.5	81.7	32.2	19.7
Average of the two highest positive SF	0.359	0.403	0.104	0.065

2.3.2 In-situ tension tests

The inverse pole figure maps of in-situ tension tests along rolling and transverse directions are shown in Fig. 2-2. The regions with high lattice curvature within a grain are apparent via gradients in the color. In both the T-RD and T-TD samples few twins formed; the twin fractions at 7% strain reach 4.6% and 4.5% respectively. The lower spread in rolling direction on the undeformed (0001) pole figure of the T-TD sample might be the reason for higher twin fraction at 1% strain (due to a resultant higher SF for slip, as was the case for the compression samples).

However, since the initial textures of both samples were fairly similar, the final twin fractions for both samples are also close after 7% strain. As shown in Fig. 2-5(a), the T-RD sample has both a higher average SF and a higher fraction of twin variants with positive SF. Hence the twin fraction may be more sensitive to the twin SF than the fraction of twin variants with positive SF.

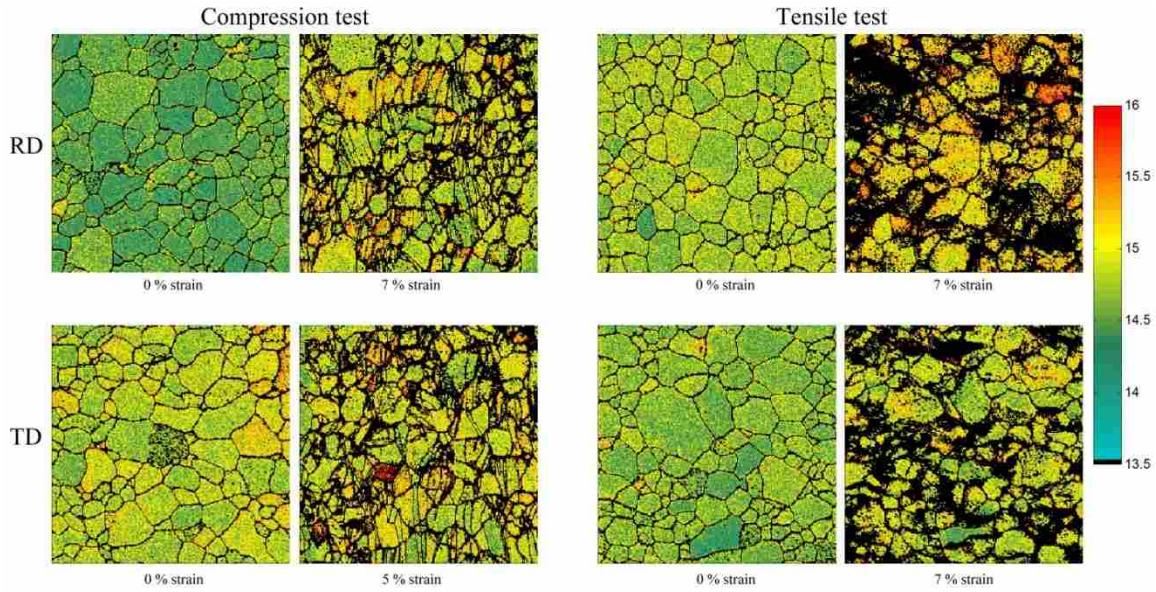

Figure 2-6. Total dislocation density maps of undeformed and final strain for different strain paths.

Total dislocation density maps of initial and 7% strained T-RD and T-TD samples in Fig. 2-6 show similar increasing rate between 0% and7% strain (2.63 times from 7.46×10^{14} to 1.96×10^{15} in T-RD sample and 2.5 times from 6.31×10^{14} *to* 1.58×10^{15} in T-TD sample). However, the increasing rates in 1% strain are different in T-RD and T-TD (1.72 times from 7.46×10^{14} to 1.29×10^{15} in T-RD sample and 1.13 times from 6.31×10^{14} to 7.1×10^{14} in T-TD sample). The initial textures of both samples have similar basal textures which spread slightly along the RD; this is more favorable for basal slip activity. Hence more slip activity and

GND generation is expected at low strain level during tensile test along RD as opposed to TD. From the maximum intensity of the (0001) pole figure in Fig. 2-4 the basal texture strengthens by 15% and 8.5% for T-RD and T-TD respectively. The strengthening of the basal texture during tension tests is reported to relate to basal slip activity [2, 4, 36].

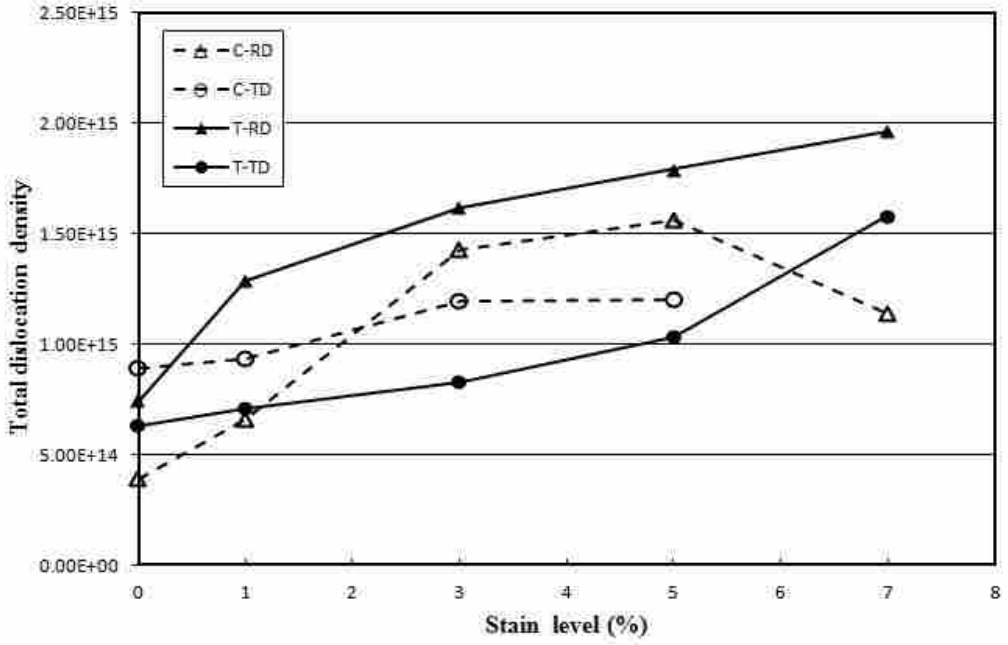

Figure 2-7. Total dislocation density plot of in-situ compression and tension tests at 0, 1, 3, 5, and 7% strains.

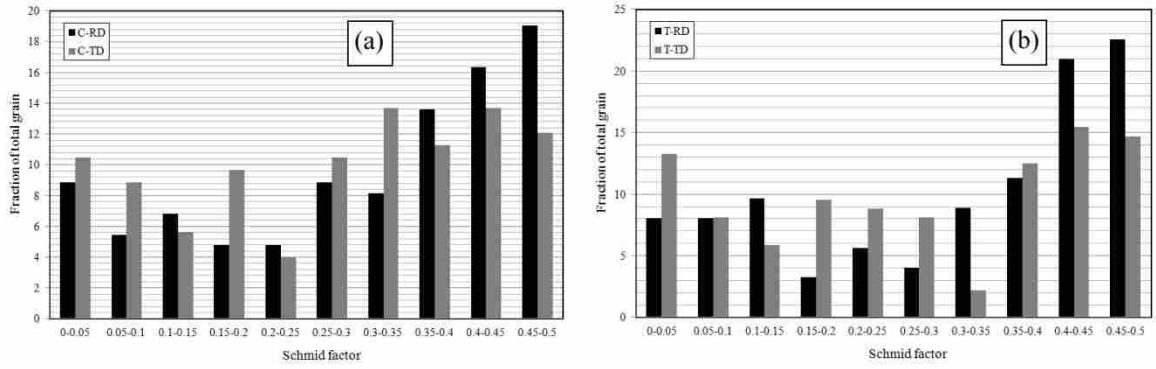

Figure 2-8. Distribution of Schmid factor values for basal slip system in C-RD and C-TD samples (a) and T-RD and T-TD samples (b).

2.3.3 Twinning vs. slip system activity

Significant differences in twin fractions between compression samples and tension samples relate to the polar nature of tensile twins. Compression in RD-TD plane leads to expansion along the ND of the sheet; because of strong basal texture of the sheet, most of the grains expand along their c-axis which favors tensile twins. As it is evident in Fig. 2-5(a) and Table 2-1, in compression tests larger fractions of possible twin variants have positive SF and the average of two highest positive SFs is higher. In Fig. 2-5(b), in compression tests most of the grains have at most 2 twin variants with negative SF value. In contrast, in tension tests, most of the grains have at least 4 twin variants with negative SF value. In contrast to the compression tests, total dislocation densities for tension tests have increasing trends. The increasing then decreasing trend for total dislocation densities of compression samples could relate to massive twin nucleation and their growth. Figure 2-9 shows three small areas containing twins. In order to have more data inside the twins, these scans were done with a 100nm step size. As it is evident in this figure, the GND content inside the twin is less than the level in the parent grain. The other reason for decreasing dislocation density in compression tests after 3% strain could relate to amount of noise in the scans at higher deformation. In other words, the regions of highest GND will have the lowest confidence index, and hence these areas will be preferentially filtered out – reducing the overall GND. However, one might notice that in tensile samples at 7% strain more data points close to the boundaries are filtered out so then the actual dislocation densities for both tension tests should be higher than the quantities in the graph. In other words, the increasing rate of GND due to deformation is higher than the decreasing rate of GND due to filtering out poor-quality points, therefore the GND contents shows an increasing rate up to 7% strain in both tension samples.

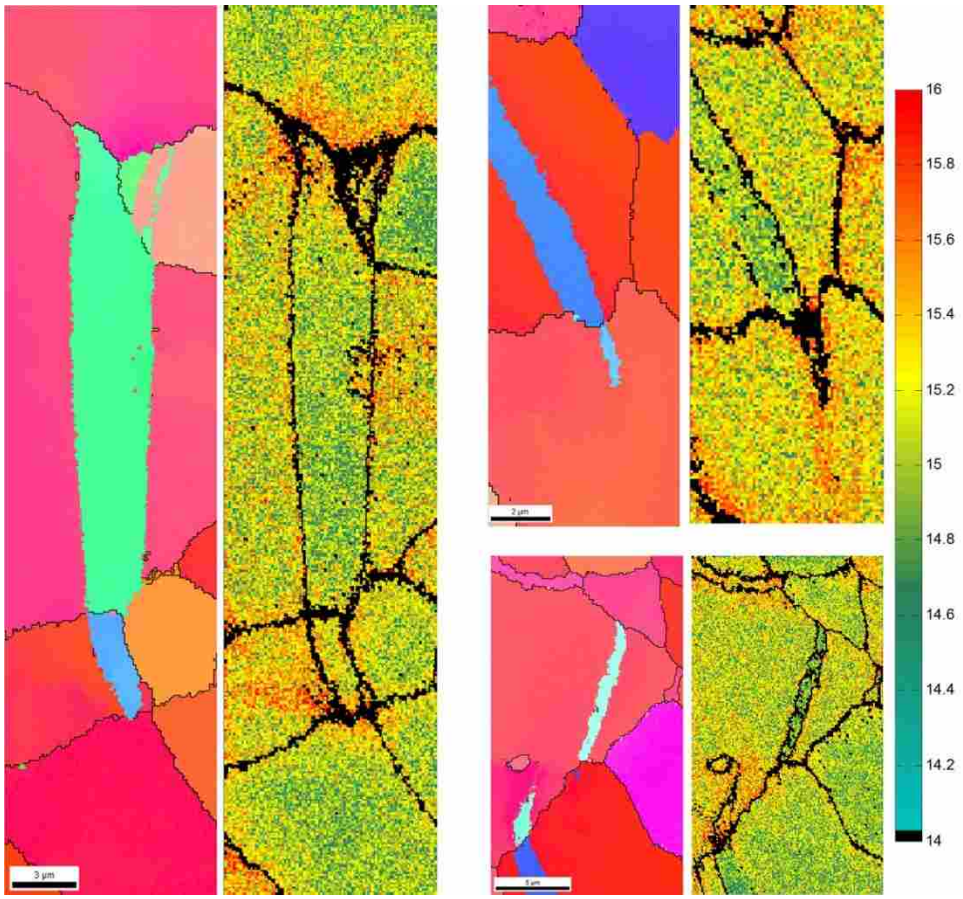

Figure 2-9. Inverse pole figure and total dislocation map of three regions with twins.

2.4 Conclusions

In-situ HR-EBSD on compression and tension tests was performed to study twin formation and dislocation evolution of AZ31 magnesium alloy along RD and TD. For in-situ compression tests, almost 25% of the total area twinned while for tension tests the twin fraction barely reached 5%. The strain threshold for twin formation is strongly depends on initial microstructure and load direction; slight deviation from basal texture will change the total average Schmid factor and the numbers of twin variants with positive SF value. Dislocation evolution also shows dependency on initial microstructure and load direction. Although the initial texture of the sample in tension test results in the same fairly close GND content, the samples loaded along RD

have sharper increase in dislocation density while loading along TD shows a modest increase of dislocation density. In compression samples, the twin formation and growth decrease the total dislocation density. This also may be affected by filtering out the highly deformed region because of low quality of EBSP.

REFERENCES

1. Gardner, C.J., et al., *EBSD-based continuum dislocation microscopy.* International Journal of Plasticity, 2010. **26**(8): p. 1234-1247.
2. Sandlöbes, S., et al., *On the role of non-basal deformation mechanisms for the ductility of Mg and Mg–Y alloys.* Acta Materialia, 2011. **59**(2): p. 429-439.
3. Agnew, S., J. Horton, and M. Yoo, *Transmission electron microscopy investigation of ⟨ c + a ⟩ dislocations in Mg and <i>α - solid solution Mg-Li alloys.* Metallurgical and Materials Transactions A, 2002. **33**(3): p. 851-858.
4. Koike, J. and R. Ohyama, *Geometrical criterion for the activation of prismatic slip in AZ61 Mg alloy sheets deformed at room temperature.* Acta Materialia, 2005. **53**(7): p. 1963-1972.
5. Koike, J., et al., *The activity of non-basal slip systems and dynamic recovery at room temperature in fine-grained AZ31B magnesium alloys.* Acta Materialia, 2003. **51**(7): p. 2055-2065.
6. Agnew, S.R., M.H. Yoo, and C.N. Tomé, *Application of texture simulation to understanding mechanical behavior of Mg and solid solution alloys containing Li or Y.* Acta Materialia, 2001. **49**(20): p. 4277-4289.
7. Wu, L., et al., *Twinning–detwinning behavior during the strain-controlled low-cycle fatigue testing of a wrought magnesium alloy, ZK60A.* Acta Materialia, 2008. **56**(4): p. 688-695.
8. Hong, S.-G., S.H. Park, and C.S. Lee, *Role of {10–12} twinning characteristics in the deformation behavior of a polycrystalline magnesium alloy.* Acta Materialia, 2010. **58**(18): p. 5873-5885.
9. Jiang, L., et al., *Influence of {10-12} extension twinning on the flow behavior of AZ31 Mg alloy.* Materials Science and Engineering: A, 2007. **445-446**(0): p. 302-309.
10. Martin, É., et al., *Variant selection during secondary twinning in Mg–3%Al.* Acta Materialia, 2010. **58**(11): p. 3970-3983.
11. Park, S.H., S.-G. Hong, and C.S. Lee, *Activation mode dependent {1 0 −1 2} twinning characteristics in a polycrystalline magnesium alloy.* Scripta Materialia, 2010. **62**(4): p. 202-205.
12. Keshavarz, Z. and M.R. Barnett, *EBSD analysis of deformation modes in Mg–3Al–1Zn.* Scripta Materialia, 2006. **55**(10): p. 915-918.
13. Koike, J., *Enhanced deformation mechanisms by anisotropic plasticity in polycrystalline Mg alloys at room temperature.* Metallurgical and Materials Transactions A, 2005. **36**(7): p. 1689-1696.

14. Agnew, S.R., et al., *Texture evolution of five wrought magnesium alloys during route A equal channel angular extrusion: Experiments and simulations.* Acta Materialia, 2005. **53**(11): p. 3135-3146.
15. Choi, S.H., E.J. Shin, and B.S. Seong, *Simulation of deformation twins and deformation texture in an AZ31 Mg alloy under uniaxial compression.* Acta Materialia, 2007. **55**(12): p. 4181-4192.
16. Agnew, S.R., D.W. Brown, and C.N. Tomé, *Validating a polycrystal model for the elastoplastic response of magnesium alloy AZ31 using in situ neutron diffraction.* Acta Materialia, 2006. **54**(18): p. 4841-4852.
17. W, P., *Resolving the geometrically necessary dislocation content by conventional electron backscattering diffraction.* Scripta Materialia, 2008. **58**(11): p. 994-997.
18. Nye, J.F., *Some Geometrical relations in dislocated crystals.* Acta metallurgica, 1953. **1**: p. 10.
19. Sun, S., Adams, B. L., and W. E. King, *Observations of Lattice Curvature Near the Interface of a Deformed Aluminium Bicrystal.* Philosophical Magazine A, 2000. **80**: p. 9-25.
20. Staroselsky, A. and L. Anand, *A constitutive model for hcp materials deforming by slip and twinning: application to magnesium alloy AZ31B.* International Journal of Plasticity, 2003. **19**(10): p. 1843-1864.
21. S. Sun, B.L.A.W.E.K., *Observations of lattice curvature near the interface of a deformed aluminium bicrystal.* Philosophical Magazine A, 2000. **80**(1): p. 17.
22. Arsenlis, A. and D.M. Parks, *Crystallographic aspects of geometrically-necessary and statistically-stored dislocation density.* Acta Materialia, 1999. **47**(5): p. 1597-1611.
23. Kysar, J.W., et al., *Experimental lower bounds on geometrically necessary dislocation density.* International Journal of Plasticity, 2010. **26**(8): p. 1097-1123.
24. Sun, S., et al., *Mesoscale investigation of the deformation field of an aluminum bicrystal.* Scripta Materialia, 1998. **39**(4-5): p. 501-508.
25. El-Dasher, B.S., B.L. Adams, and A.D. Rollett, *Viewpoint: experimental recovery of geometrically necessary dislocation density in polycrystals.* Scripta Materialia, 2003. **48**(2): p. 141-145.
26. Brent L. Adams, J.K., *EBSD-Based Microscopy: Resolution of Dislocation Density.* Computers, Materials, & Continua, 2009. **14**(3): p. 12.
27. John Price Hirth , J.L., *Theory of Dislocations*1975: McGraw-Hill. 780.
28. Yoo, M., *Slip, twinning, and fracture in hexagonal close-packed metals.* Metallurgical and Materials Transactions A, 1981. **12**(3): p. 409-418.
29. Huber, J.H., M., *Nucleation of recrystallized grains in heavily cold-worked α-brass.* Metal Science, 1979. **13**(12): p. 5.
30. Juergen Huber , M.H., *NUCLEATION AND ANNEALING TEXTURE DEVELOPMENT IN ROLLED 70:30 BRASS.* Materials Research and Advanced Technique, 1980. **71**(1): p. 6.
31. Wu, L., et al., *Internal stress relaxation and load redistribution during the twinning–detwinning-dominated cyclic deformation of a wrought magnesium alloy, ZK60A.* Acta Materialia, 2008. **56**(14): p. 3699-3707.
32. Bohlen, J., et al., *The texture and anisotropy of magnesium–zinc–rare earth alloy sheets.* Acta Materialia, 2007. **55**(6): p. 2101-2112.

33. Godet, S., et al., *Use of Schmid factors to select extension twin variants in extruded magnesium alloy tubes.* Scripta Materialia, 2006. **55**(11): p. 1055-1058.
34. Jiang, L., et al., *Twinning and texture development in two Mg alloys subjected to loading along three different strain paths.* Acta Materialia, 2007. **55**(11): p. 3899-3910.
35. Miles, M., et al., *Room Temperature Ductility and Microstructure of Magnesium AZ31B Sheet.* Journal of Materials Engineering and Performance, 2011. **20**(8): p. 1357-1363.
36. Kocks, U.F., C.N. Tomé, and H.-R. Wenk, *Texture and anisotropy : preferred orientations in polycrystals and their effect on materials properties*1998, Cambridge, U.K.; New York: Cambridge University Press.